Results From Five *Chandra* Observations of the Normal Galaxy NGC 3877

by

Edgar Raul Gonzalez

Submitted to the Department of Physics
in partial fulfillment of the requirements for the degree of

Bachelor of Science in Physics

at the

MASSACHUSETTS INSTITUTE OF TECHNOLOGY

June 2004

Author ..... 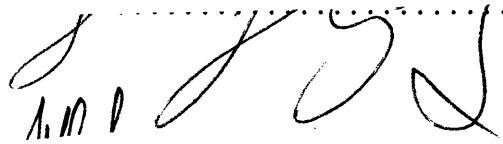
Department of Physics
May 21, 2004

Certified by 5/22/04
Walter H.G. Lewin
Professor, Department of Physics
Thesis Supervisor

Accepted by 5/24/04
David E. Pritchard
Thesis Coordinator, Department of Physics

Results From Five *Chandra* Observations of the Normal Galaxy NGC 3877

by

Edgar Raul Gonzalez

Submitted to the Department of Physics
on May 21, 2004, in partial fulfillment of the
requirements for the degree of
Bachelor of Science in Physics

Abstract

We present the results of five *Chandra* observations of the normal galaxy NGC 3877. A total of 27 X-ray sources are detected, including SN 1998S. We find 15 sources to be variable during the 646-day period covered by the observations. We use two methods to determine source color and find no apparent correlation between color and brightness in our population sample. We provide flux and luminosity estimates for every source and construct cumulative X-ray luminosity functions (XLFs) for each observation. We find a higher density of luminous ($\sim 10^{37}\,\mathrm{erg\,s^{-1}}$) sources in NGC 3877 than we see in two other galaxies. We tentatively identify some sources as X-ray binaries.

Thesis Supervisor: Walter H.G. Lewin
Title: Professor, Department of Physics

Contents

List of Figures

List of Tables

Chapter 1

Introduction

The Chandra X-ray Observatory observed the normal galaxy NGC 3877 five times over two years. Multiple observations offer a treasure trove of science: we can investigate the *evolution* of source properties, and we can evaluate the methods used to characterize source and galactic properties from single observations.

We prepare the reader for the ensuing investigation by introducing the historical, morphological and technical tools needed to appreciate this work. We begin from scratch: What are X-rays? How are they made? And we end by motivating the usefulness of, need for and excitement in studying the X-ray sky.

1.1 X-rays and their Plenitude

Astronomy is historically based on light, or electromagnetic radiation. Astronomers deal with light in three ways: they measure its intensity (over a wavelength range), they study its spectrum, and they determine its polarization. From this they infer the physical properties of light-producing sources.

Our wavelength range of interest corresponds to the part of the electromagnetic spectrum occupied by X-rays. X-rays are a highly energetic form of electromagnetic radiation with wavelengths $10^{-3}\,\mathrm{nm} \lesssim \lambda_x \lesssim 10\,\mathrm{nm}$ and corresponding photon energies

of $0.1\,\mathrm{keV} \lesssim E_x \lesssim 10^3\,\mathrm{keV}$.

1.1.1 Discovery

In 1895 November the German physicist William Röntgen observed that a sheet of paper coated with Barium platinocyanide glowed when a nearby cathode ray tube was turned on. The paper glowed even when he placed (thin) metal plates between the paper and the cathode. Not knowing the nature of this radiation, Röntgen dubbed it "X"-radiation[3].

1.1.2 What are they?

The first non-visible form of electromagnetic radiation (radio) was discovered by the German physicist Heinrich Hertz in 1888, less than ten years before Röntgen's discovery. Röntgen suspected X-rays were also a new form of electromagnetic radiation; but, as he could neither reflect them nor produce interference patterns, he was unable to prove it.

Another German physicist, Max von Laue, proposed the following explanation for Röntgen's failure to observe X-ray reflection or interference: X-ray frequencies were so high and their wavelengths so small ($\sim$atom) that they could only reflect if the grazing angle were small and the reflecting surface very smooth. Otherwise they would scatter. He further suggested that the layers of atoms in a crystal would be closely enough spaced to produce interference patterns.

Laue's colleagues Walther Friedrich and Paul Knipping tested his suggestion and produced an X-ray interference pattern. Von Laue worked out the mathematical formulation of it, and the discovery was published in 1912. This proved that X-rays were in fact a high-frequency, short-wavelength form of non-visible light.

Albert Einstein proposed (correctly) in 1905 that electromagnetic waves were not continuous but were instead comprised of discrete bundles of pure energy called pho-

tons. Photon energies would be proportional to the wave's frequency and inversely proportional to its wavelength.

Röntgen was awarded the first Nobel Prize for Physics in 1901 for his discovery of X-rays[1]. Laue received the 1914 Nobel Prize for Physics for his work on diffraction of X-rays on crystals.

1.1.3 Generating X-radiation

Their high frequencies and, consequently, their high energies make X-rays a useful tool in the investigation and characterization of matter.

X-rays are generated when high-energy electrons are slowed by an atom's nucleus. Accelerated charges give off electromagnetic radiation, and when the energies of the bombarding electrons are high enough, the emission is in X-rays. This radiation is called "bremsstrahlung." It is characterized by a continuous distribution of radiation which becomes more intense and shifts toward higher frequencies when the energy of the bombarding electrons is increased.

When moving charges spiral in a magnetic field, they produce radiation as a result of their acceleration. This radiation is called "synchrotron radiation" and has been observed in astronomical sources, such as the Crab Nebula. Its signature is that of a power law.

"Thermal radiation" is electromagnetic radiation emitted by an object as a result of its temperature (the thermal motion of its constituent particles). The higher the temperature, the faster the motion of the particles and the higher the energy of the radiated photons. For temperatures above 10^6 K, these photons are predominantly X-rays.

X-rays are energetic enough to eject electrons from an atom's inner shells. The consequent vacancy is filled by an electron from a higher energy level, leaving a vacancy in its shell that is in turn filled by another electron, and so on. As electrons

[1]It should be noted that he declined to seek patents or proprietary claims on his discovery.

drop from outer shells to shells closer to the nucleus, they emit "characteristic X-rays," whose energies equal the difference in binding energies between the shells. The process of emission of characteristic X-rays is called "X-ray fluorescence."

If an incident X-ray scatters off an electron, it will lose or gain energy and emerge from the collision with a shifted frequency. This radiation is called "Compton radiation."

The four main astrophysical mechanisms for generating X-rays are[4]: thermal bremsstrahlung (from hot gases), synchrotron radiation (from highly energetic electrons of $\sim 10^4$ GeV), thermal radiation (star-like objects) and Compton scattering.

1.2 X-ray Astronomy

X-rays have posed many challenges for those whose interests lie skyward. First, X-rays do not penetrate the Earth's atmosphere. Even from mountain tops, X-ray observations are useless[5]. At first, the only way to observe cosmic X-rays was to put a detector high above the Earth on a balloon or rocket.

Telescopes provided the second challenge. As Röntgen discovered, X-rays are difficult to reflect and therefore difficult to focus. Much like skipping a pebble on a lake, X-rays would reflect only for small grazing angles. The German physicist Hans Wolter published a paper in 1952 in which he showed that not one, but two reflections were needed to produce a two-dimensional image. The mirror, however, remained an engineering challenge as it needed to be uniform to within a few tens of atoms.

1.3 X-ray Sources

Some fifty years after X-rays were discovered by Röntgen, the Sun became the first detected extraterrestrial X-ray source. In the ensuing fifty years more than 60,000

Table 1.1: The number of X-ray sources known throughout the years. Consecutive columns give the year, the number of X-ray sources known at that year, and the basis for the number.

Year	Sources	Based on
1950	1	Rocket experiment
1960	2	Nothing
1962	3	Rocket experiments
1965	11	Rocket experiments
1970	60	Rocket & balloon experiments
1974	160	3rd *Uhuru* Catalog
1980	680	Amnuel et al. (1982) Catalog
1984	840	HEAO A-1 Catalog
1990	8,000	*Einstein* & *EXOSAT* source catalogs
2000	220,000	*ROSAT* source catalogs
2003	500,000	*XMM-Newton* & *Chandra*
2010	3,000,000	Predicted

X-ray sources were detected. Table 1.1[2] lists the number of X-ray sources known throughout the years.

1.3.1 The Beginning

The Sun is our solar system's strongest emitter of X-rays with a typical $0.1 - 2.4\,\mathrm{keV}$ luminosity of $L_x \approx 10^{27}\,\mathrm{erg\,s^{-1}}$[6]. It was detected as an X-ray source in 1949[7].

Its detection, however, caused many scientists to lose interest in the search for other X-ray sources[8]. The sun was detected because of its proximity. X-ray emission comparable to the Sun's from the nearest stars would go undetected unless instruments improved their sensitivity by a factor of 100,000[8]. An X-ray source at a distance of 1 kpc would need to produce 10^{11} times the luminosity of the Sun in order to be detected in 1960.

This attitude changed after 1962, when a rocket-borne experiment intended to

[2]This information is as of 2003 August 25 and provided by NASA's High Energy Astrophysics Science Archive Research Center. http://heasarc.gsfc.nasa.gov/docs/heasarc/headates/how_many_xray.html

search the Moon for X-rays failed to detect any lunar X-rays but did detect the first cosmic X-ray source[9]. It was subsequently found to be in Scorpius[10] and called Scorpius X-1[11], or Sco X-1 for short. Further observations confirmed the point-like nature of Sco X-1[12] and detected other cosmic X-ray sources[13]. These were a wholly new and unpredicted class of astrophysical objects.

1.3.2 Other Sources

Other objects in our solar system which have been detected as X-ray emitters include the Moon, the planets Jupiter, Saturn, Venus, and Mars, some of the moons of Jupiter, and the Io Plasma Torus, as well as a number of comets.

In our Galaxy, the brightest X-ray emitters (with $L_x \lesssim 10^{39}\,\mathrm{erg\,s^{-1}}$) are X-ray binaries (XRBs) and supernova remnants. The most luminous X-ray sources in the universe are rich clusters of galaxies and active galactic nuclei (AGN), both of which can reach X-ray luminosities as high as $L_x = 10^{45}\,\mathrm{erg\,s^{-1}}$. Typical "normal" galaxies, on the other hand, have much lower X-ray luminosities lying in the range from $10^{38}\,\mathrm{erg\,s^{-1}}$to $3 \times 10^{42}\,\mathrm{erg\,s^{-1}}$.

1.3.3 X-ray Binaries

X-ray binaries consist of a normal star and a compact object (black hole, neutron star, or white dwarf). If the two stars are close enough, matter from the normal star can flow to the compact object and form an accretion disk. The material accelerates in the gravitational field of the compact object, and viscous heating in the disk leads to temperatures of millions of Kelvin. The material radiates thermal X-rays. *ROSAT* and *Chandra* are finding an increasing number of these systems in other galaxies.

1.3.4 X-ray Transients

The class of sources called "transients" was created to distinguish them from the more permanent, stable sources observed in the X-ray sky. X-ray transients seem to divide themselves naturally into 2 classes: those associated with High Mass X-ray Binaries (HMXBs) and those associated with Low Mass X-ray Binaries (LMXBs). The HMXBs contain a neutron star or black hole paired with a massive star ($\gtrsim 5M_{\odot}$). The emission from these systems is characterized by a hard spectrum. LMXBs contain a neutron star or black hole and a low mass star. LMXBs often have a soft spectrum.

1.3.5 Supernova remnants

Supernova remnants are hot gases that have been hurled through space by a supernova explosion. Remnants can be thousands of years old and many hundreds of light years in size. The various gases in the remnant are energetic enough to emit characteristic X-rays, which lead to narrow features in its spectrum, called emission lines. The materials present can be identified by these emission lines.

The observed spectra from supernova remnants are composed of emission lines plus some broad and usually constant emission. This underlying emission could be thermal emission from its gases. Or it could be synchrotron emission from energetic cosmic rays accelerated in magnetic fields.

1.4 Observatories

X-ray astronomy has seen an improvement in sensitivity in the last 40 years equivalent to that of going from the naked eye to the Keck Observatory.

Table 1.2: Notable X-ray satellites. Consecutive columns give the satellite, its launch date, the date of its demise, its energy range in keV, its best spatial resolution, its field of view (FOV), and its limiting sensitivity in units of $\mathrm{erg\,cm^{-2}\,s^{-1}}$.

Satellite	Launch	Demise	Energy	Res.	FOV	Sensitivity
Uhuru	1970 Dec	1975 Jan	2.0-20	30'	$5.2^o \times 5.2^o$	$\sim 10^{-11}$
SAS-3	1975 May	1979 Apr	0.15-1		$2.9^o \times 2.9^o$	$\sim 10^{-11}$
HEAO-1	1977 Aug	1979 Jan	0.2-15	2'	$\sim 1^o \times 4^o$	$\sim 10^{-12}$
Einstein	1978 Nov	1981 Apr	0.4-4	60"	$75' \times 75'$	$\sim 10^{-14}$
ROSAT	1990 Jun	1999 Feb	0.1-2.5	5"	$38' \times 38'$	$\sim 10^{-14}$
ASCA	1993 Feb	2001 Mar	0.4-12	60"	$24' \times 24'$	$\sim 10^{-14}$
Chandra	1999 Jul	$\sim$ 2009	0.1-10	<1"	$17' \times 17'$	$\sim 10^{-16}$
XMMN	1999 Dec	$\sim$ 2009	0.1-15	6"	$30' \times 30'$	$\sim 10^{-16}$

1.4.1 Balloons & Rockets

The period from the time of the discovery of Sco X-1 to the launch of the first X-ray astronomy satellite, *Uhuru*, in 1970 yielded ~60 cosmic X-ray sources. These included two sources which had been identified with optical counterparts[14],[15]; six supernova remnants[16]; the Large Magellanic Cloud[17]; active galaxies M87[18] and NGC 5128[19]; the Coma Cluster[20]; and the quasar 3C273[18].

1.4.2 Uhuru

Uhuru was the first earth-orbiting mission dedicated entirely to X-ray astronomy. It was launched in 1970 December 12 and operated until 1973 March. With a 10-fold improvement in sensitivity over earlier rocket missions[21], *Uhuru* detected 339 X-ray sources: XRBs, supernova remnants, Seyfert galaxies and clusters of galaxies.

1.4.3 The Einstein X-Ray Observatory

Einstein was the first fully imaging X-ray telescope dedicated to cosmic X-rays put into space. It was launched on 1978 November 12 and operated until 1981 April. A 1000-fold improvement in sensitivity over *Uhuru*, along with a high angular resolu-

tion (10") and a large $75' \times 75'$ field of view (FOV), made *Einstein* the first to image extended objects and diffuse emission and allow for high resolution spectroscopy of supernova remnants. *Einstein's* detections of hot gas in clusters of galaxies strengthened the argument for "dark matter,"[3] affirming X-ray astronomy's position in mainstream astronomy[5]. All in all *Einstein* gathered data on more than 5,000 X-ray sources.

1.4.4 Röntgen Satellite Project

ROSAT, with twice the collection area of *Einstein*, was designed to perform the first deep survey of the whole sky in soft X-rays (0.1-2 keV). It was launched on 1990 June 1 and operated until 1999 February. Its X-ray all-sky survey catalog contains more than 150,000 sources–about 30 times more than had been previously known. *ROSAT* was the first to detect X-ray emission from comets and the Moon[22].

1.4.5 The Advanced Satellite for Cosmology and Astrophysics

ASCA was the first satellite to use CCD detectors for X-ray astronomy. The satellite was launched on 1993 February 20 and operated until 2000 July 15. With a spectral resolution eight times that of *ROSAT*, *ASCA* determined the nature of newly discovered sources and allowed for detailed spectroscopy of, for example, interacting binaries.

1.4.6 The X-Ray Multi-Mirror Mission

XMM-Newton was launched on 1999 December 10. Its large collecting area and ability to make long uninterrupted exposures provide highly sensitive observations—a 10^5 improvement over *Uhuru*. Its 1XMM catalogue (ver. 1.0.1), released on 2003 April, lists more than 50,000 serendipitous X-ray sources.

[3]The measured gravitational force in clusters of detected matter (gas and stars) is not sufficient to keep the gas from escaping.

1.5 *Chandra*

The *Chandra X-Ray Observatory* combines an efficient, high-resolution ($\leq 1/2$ arcsecond) X-ray telescope with a suite of advanced imaging and spectroscopic instruments. The Observatory was launched by NASA's Space Shuttle *Columbia* on July 23, 1999.

Chandra was designed to provide order-of-magnitude advances over previous X-ray astronomy missions with regards to spatial and spectral resolution. The High Resolution Mirror Assembly (HRMA) produces images with a spatial resolution $\lesssim$0.5 arcsec.

1.6 Previous Work

Before embarking on our investigation, we describe some of the questions raised and answered by previous studies of galaxies and their X-ray emission.

1.6.1 Classification by Spectra

Spectra have been used to identify X-ray sources as well as galactic regions[23]. *Chandra's* spectral resolution allows for detailed analysis of source emission. Unfortunately, the sources in this study are too faint to be identified by their spectra. Still, we can look for trends: are brighter sources harder?

1.6.2 Long-Term Variability

Though repeated *Chandra* observations of a galaxy have been scarce, interesting findings have been reported on the long-term variability of X-ray sources.

Chandra observed NGC 1637 seven times and found every source to be variable[24]. Fifty percent of M31's X-ray sources with luminosities $L_x \gtrsim 5 \times 10^{36}\,\mathrm{erg\,s^{-1}}$have been found to be variable[25]. If we limit the sample to sources with $L_x \gtrsim 10^{37}\,\mathrm{erg\,s^{-1}}$,

which is similar to the detection threshold of our observations, the fraction of variability can be as high as 80 percent over two years[26].

Is this variability common to other galaxies? If so, how well can they be characterized by single observations?

1.6.3 X-ray Luminosity Functions

XLFs are thought to reflect the formation, evolution and physical properties of the X-ray source population in a galaxy[27]. XLF slopes have been related to population age[28], parent galaxy type[29] and star formation rate[30].

If galactic sources are variable, would the host galaxies have variable XLFs as well?

Chapter 2

Observations

This chapter describes the five *Chandra* observations of NGC 3877, providing observation dates, exposure times, aim points and instrumentation details.

On 1999 October 28, radio observations triggered[31] a *Chandra* observation of the supernova (SN) 1998S[1] in NGC 3877. SN 1998S was subsequently observed five times over a span of 646 days. Though these observations targeted the supernova, they also included its host galaxy. The supernova has been studied extensively (e.g., Pooley et al.[31]). We concern ourselves here with the galaxy.

2.1 What, when, where, why & how

NGC 3877 was observed five times with the Advanced CCD Imaging Spectrometer (ACIS) instrument on board the *Chandra X-Ray Observatory* for a total of 120.1 ks. Observations took place on January 10 (Obs. ID 767), March 7 (768) and August 1 (952) of 2000 and January 14 (1971) and October 17 (1972) of 2001. A summary of the observations is given in Table 2.1.

Each observation placed SN 1998S near the aim point of *Chandra's* back-side-illuminated S3 chip. The galaxy fit completely within the $8\farcm4 \times 8\farcm4$ view of the S3

[1]SN 1998S is a Type IIn supernova located 16" west and 46" south of the galactic nucleus[32]. It was discovered on 1998 March 3.

Table 2.1: *Chandra* observations of NGC 3877. Consecutive columns give the observation number; identification (ID); date; starting UTI time; aimpoint's right ascension (RA) in units of hours, minutes and seconds; aimpoint's declination (DEC) in units of degrees, minutes and seconds; total length in units of ks; and the filtered length in units of ks.

				Aimpoint		Exposure Time	
Obs.	ID	Date	Time	RA	DEC	Total	Net
1	767	2000 Jan. 10	18:23:09	11:46:06.75	47:29:33.77	18.9	18.0
2	768	2000 Mar. 07	19:22:28	11:46:06.75	47:29:07.76	23.5	22.3
3	952	2000 Aug. 01	06:51:11	11:46:06.85	47:28:18.21	19.8	19.1
4	1971	2001 Jan. 14	19:27:35	11:46:06.44	47:29:33.98	29.2	27.7
5	1972	2001 Oct. 17	03:02:24	11:46:09.45	47:29:06.43	28.7	26.8

chip.

The data were taken in what is called "timed-exposure" mode, in which a CCD collects data for a preselected amount of time – the frame time – before reading it out. Since the readout process lasts 3.2s regardless of frame time, frame times shorter than 3.2s necessarily result in time where no data is taken. Frame times longer than 3.2s increase the probability of pileup[33] – when multiple photons are detected in the same pixel during the same frame time and are thus confused for a single event. The nominal frame time of 3.2s was used for each observation.

2.2 On-Board Processing

Not every incident X-ray is registered as an event. *Chandra's* on-board processing selects events based on the pixel value (energy) induced by the incident X-ray. First, the pixel value must exceed ~0.7 eV (this energy is called the event threshold). Secondly, the pixel value must exceed the pixel values of all its surrounding pixels (i.e., it is a local maximum).

Once a pixel passes the above criteria, its surrounding 3×3 pixels get compared to the event threshold. Each neighboring pixel that exceeds the event threshold is assigned a bitwise number that corresponds to its relative position to the central event

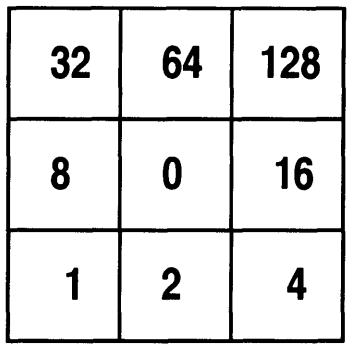

Figure 2-1: ACIS event grades are assigned by summing the numbers corresponding to each neighboring pixel that exceeds the event threshhold. The bitwise numbering scheme allows the sum to uniquely specify which neighboring pixels exceed the event threshold. For example, a single-pixel event has an ACIS grade of 0, an event with a grade of 255 has all of its surrounding pixels exceeded the event threshhold, while a grade of 5 means that only the pixles at the lower right and left corners exceed the event threshold. Grades help filter background and unwanted events from telemeterized data and thus reduce bandwidth.

pixel. For example, the upper left corner is assigned the number 32, the lower right corner is assigned the number 4. The sum of the numbers assigned to the neighboring pixels is called the event's ACIS "grade," and it uniquely determines which of the surrounding pixels exceeded the event threshold. For example, had just the pixels in the upper left corner and lower right corner exceeded the event threshold, the event would have an ACIS grade of 36. The grade characterizes the significance of the event[34].

Figure 2-1 illustrates the grade-assigning scheme. Grades are used by telemetry formats to improve the signal-to-noise ratio of the data transmitted to Earth.

The Faint (F) telemetry format transmits for each event its position in detector coordinates, arrival time, energy, and the contents of the 3×3 island that determines the event grade. All five observations were transmitted in this format.

Chapter 3

Data Reduction

In this chapter we describe the procedure for preparing the transmitted data for analysis (e.g., removing intervals of background flaring from the data). We follow the data-preparation and source-detection threads provided by the *Chandra* X-Ray Center[35]. The data were reprocessed using the *Chandra* Interactive Analysis of Observations (CIAO) software (ver. 3.2) package with calibration products (CALDB; ver. 2.8). CIAO software packages are *italicized.*

3.1 A quick note on clarity

Because each observation underwent the same procedures, we will refer to just one observation in the following description to avoid repetition. For instance, when we say we checked for background flares we mean that we checked for background flares *in each observation.* Any differences among observations will be noted.

3.2 Getting to the Level 2 Event Files

Chandra characterizes each X-ray event with the energy of the incident photon, the time of detection, a grade (see Sec. 2.2), and two position coordinates. This infor-

mation is stored in event files. Further information essential to the observation (e.g., the telescope's pointing position vs. time) are stored in other files (e.g., the aspect solution file).

Each file has a level associated with it that describes the extent of processing that went into making it. Processing levels range from 0 to 3, but we need only concern ourselves here with level 1 and level 2 files. Level 1 products contain calibrated data derived from a single observation interval (i.e., as if the observation had a constant calibration). We began by downloading the level 1 products for each observation. Level 2 products contain merged (and in our case filtered) data from all intervals of an observation. It is therefore the level 2 event file that we must work with.

3.2.1 The Level 1 Event File

The level 1 event file does not contain the actual event energies; instead it contains Pulse Height Amplitudes (PHA), which are related to energy by the detector's gain map. We ran *acis_process_events* with the latest gain map on the level 1 event file to produce a new level 1 event file that contained energy information. This also corrected for charge transfer inefficiency (CTI), the loss of charge from pixels as their signal travels from one pixel to the next during readout. We deviated from the standard data processing by *not* randomizing the pixel locations of events as pixel randomization lowers spatial resolution. We now had a preliminary level 2 event file that needed to be filtered for background flares (see Sec. 3.2.3.

3.2.2 Regions of Interest

To ensure uniformity across the five data sets we confined our investigation to a $6\farcm3 \times 6\farcm3$ region in the sky that was completely covered by each observation and contains the galaxy. Fig. 3-1 shows this region of interest (ROI), an ellipse we defined to delineate the galaxy (NGC 3877), and a background region.

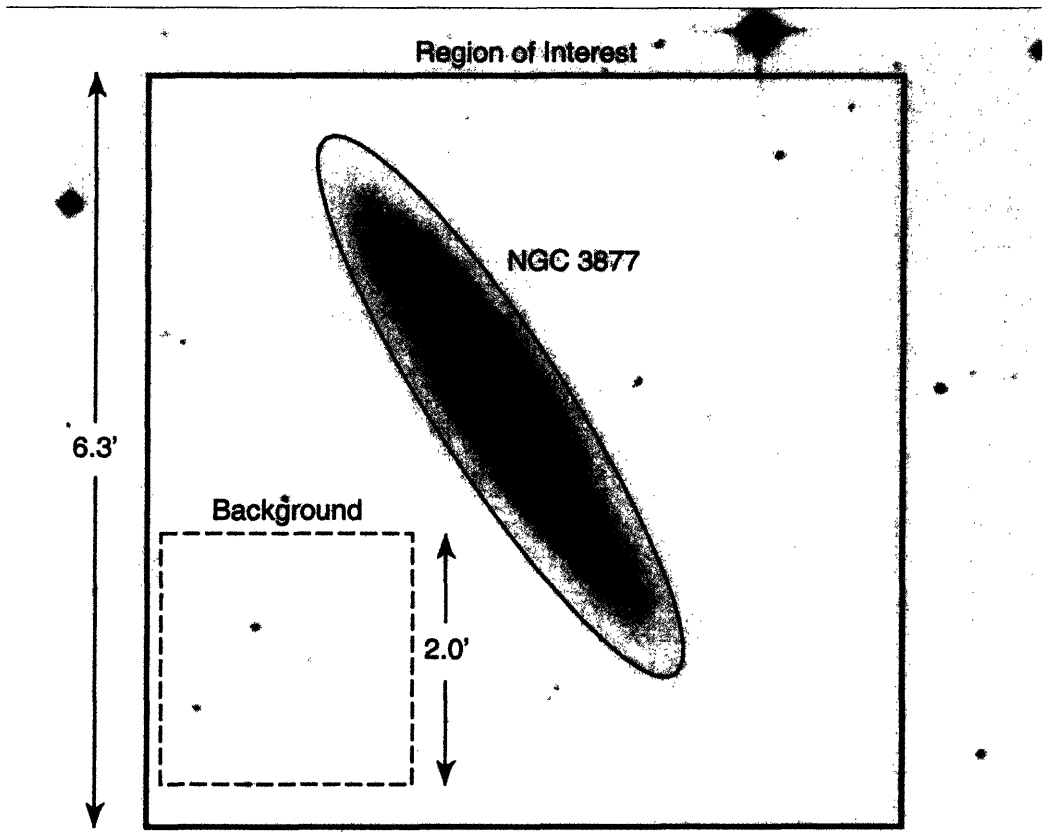

Figure 3-1: This figure shows some critical regions overlayed on an optical image from the *Space Telescope Science Institute Digital Sky Survey.* Data were extracted from the $6'.3 \times 6'.3$ region labelled "ROI." A $2' \times 2'$ box away from the galaxy was used as the background region.

3.2.3 Background Flares

The quiescent ACIS X-ray background consists of a relatively soft contribution from the Cosmic X-ray Background (CXB) and a hard (> 5 keV) contribution from cosmic ray-induced events[36]. There are standard procedures for dealing with background noise. Signal-to-noise ratios are usually either improved or they are used to flag and remove data (e.g., by applying the GTI file). Either way data is not corrupted by the ACIS X-ray background.

Background flares, however, demand special attention as they can increase the total count rate by a factor of 100[37]. These flares have been observed everywhere

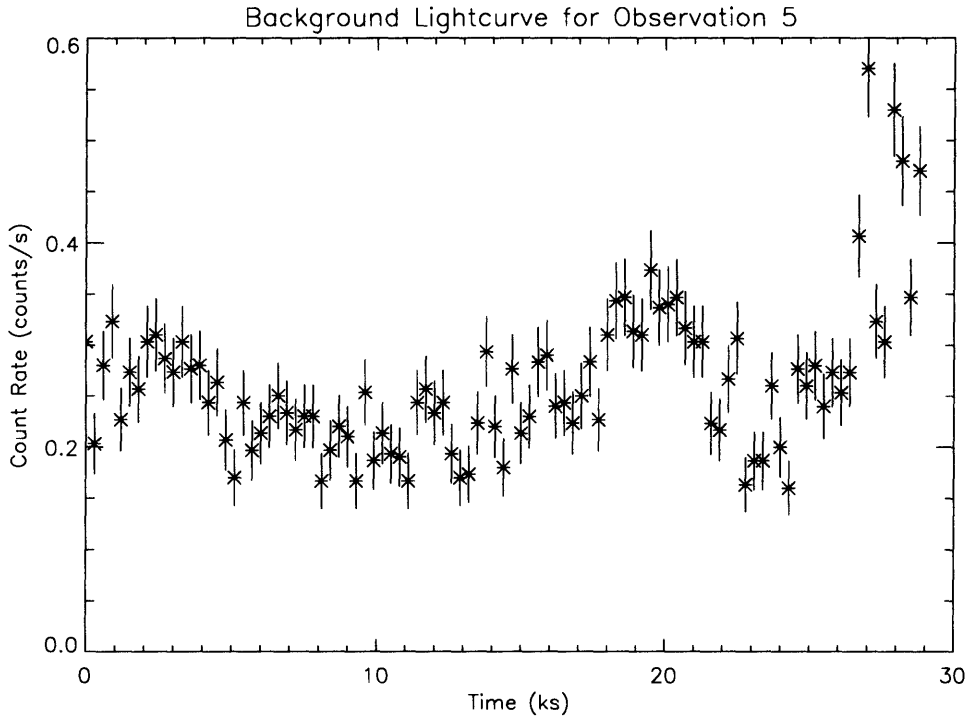

Figure 3-2: This lightcurve of the background in observation 5 shows a flare beginning at 27 ks and lasting for the rest of the observation. Periods of background flaring were filtered from the data.

in the *Chandra's* orbit. While the nature of these flares remains undetermined, there is a simple procedure to deal with them. Namely, we exclude periods of flaring from the data.

To filter the data, we chose for the background a source-free (as estimated by visual inspection) region away from the galaxy so not to confuse source variations for background flares. Figure 3-1 shows the selected background region. We then used *dmextract* to create a lightcurve (counts vs. time) of the region, with data separated into $300\,s$ bins as a compromise between resolution and signal-to-noise.

Background lightcurves were analyzed with *analyze_ltcrv.sl*, which performs an iterative sigma-clipping algorithm, removing at each iteration all points more than $\pm 3\sigma$ from the mean until all data points lie within $\pm 3\sigma$ of the mean. Figure 3-2 shows the lightcurve from Obs. 5, which shows a flare toward the end of the observation.

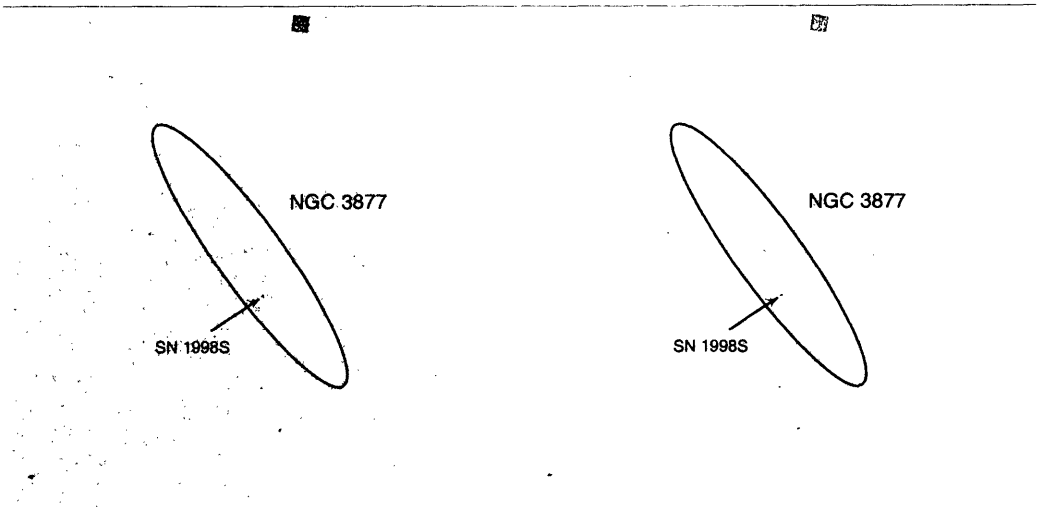

Figure 3-3: Obs. 4's level 1 event file is shown on the left, and its level 2 events file is shown on the right. The level 2 file has been filtered for background noise.

Periods of high background were input into *dmgti* to make a new GTI file. The final level 2 event file was made with *dmcopy* by filtering the preliminary level 2 event file with the GTI file and limiting events to those located in the ROI. Fig. 3-3 compares the images from level 1 and 2 event files from Obs. 4.

3.3 Preparing to Find Sources

Chandra, by design, does not give each point in the sky the same attention. As it dithers, its pointing position changes (so to average across calibration uncertainties[1]). Because the detector is not uniform, the exposure received by a point in the sky is dependent on the corresponding detector position. Before searching the sky for X-ray sources we must therefore re-scale events to the same relative exposure.

The telescope's pointing position is stored in the aspect (pointing position vs. time) solution file. We ran *asphist* using the aspect solution file to detail the aspect history of the S3 chip. We made an instrument map (effective area vs. detector

[1]Dithering also keeps one bad pixel from ruining an entire observation.

position[2]) using *mkinst*.

The aspect histogram and instrument map files were input into *dmexpmap* to produce an exposure map. The exposure map is essentially an image of the effective area at each sky position, accounting for the effects of dither motion. Exposure-corrected images were made with *dmimgcalc* in the soft (0.5-1.2 keV), hard (1.2-8.0 keV) and broad (0.5-8 keV) energy bands.

Having transformed the level 1 data into exposure-corrected images, it was now sufficiently reduced to be analyzed. The following chapter details the analysis and lists the results.

[2]More specifically, an instrument map is the product of the mirror effective area projected onto the detector surface with the detector quantum efficiency (QE) taken into account.

Chapter 4

Results

In this chapter we describe our analysis of the reduced data and present the consequent results. We locate point-like X-ray sources and compute some of their properties (e.g., photon counts, count rate, spectral color, flux and luminosity). We also describe X-ray source *populations* with Log(N)-Log(S) curves and cumulative X-ray luminosity functions (XLFs).

4.1 A quick point on clarity

As the analysis for each observation is similar, we will refer to just one observation in the following description to avoid repetition. Results from each data set will of course vary. We will therefore list the results from each observation.

4.2 X-ray Sources

We searched the data for point-like X-ray sources using the source-detection tool *wavdetect* to construct a list of source locations and sizes. We eliminate from further analysis those sources outside of NGC 3877.

4.2.1 Finding X-ray Sources in NGC 3877

Wavdetect[38] uses an iterative "Mexican-Hat" wavelet detection algorithm to detect and characterize X-ray sources. We ran *wavdetect* using the exposure map on the level 2 events file to search for point-like X-ray sources in the soft (0.5-1.2 keV), hard (1.2-8.0 keV) and broad (0.5-8 keV) energy bands of each observation. We did the same with a merged observation.

Wavdetect found a total of 25 sources in the first observation, 36 in the second, 35 in the third, 38 in the fourth and 33 in the fifth. A merged image had 54 sources detected. We identified sources by their location and determined that a total of 57 unique sources had been detected in the observations. Table A.1 lists (galactic) source locations and detections. SN 1998S is Src. 1.

We constructed an ellipse around an optical image[1] of NGC 3877 and defined its interior to be the galaxy. The galaxy contained 27 of the 57 detected sources. Fig. 4-1 shows the sources inside the galaxy.

4.2.2 Accounting for Background Objects

It is unlikely that all 27 sources are associated with the galaxy. X-ray sources directly behind (i.e., farther away) the galaxy could be bright enough to shine through the galaxy and be detected. These background objects may, for example, be Active Galactic Nuclei (AGNs). The 30 X-ray sources detected outside of the galaxy are either background or foreground objects.

We used two statistical methods to account for these objects. First we calculated the source density $\rho_{out} = 0.858\,\mathrm{srcs/arcmin^2}$ outside of the galaxy and applied it inside the galaxy. This gave an estimate of 4 background objects inside the galaxy.

This is an underestimated number of background objects because *Chandra's* sensitivity decreases with separation from the aim-point, making detections of sources

[1]The image is from the *Space Telescope Science Institute Digital Sky Survey.* The 4.2 ks observation was taken by the Palomar 48-in Observatory on 1995 April 25

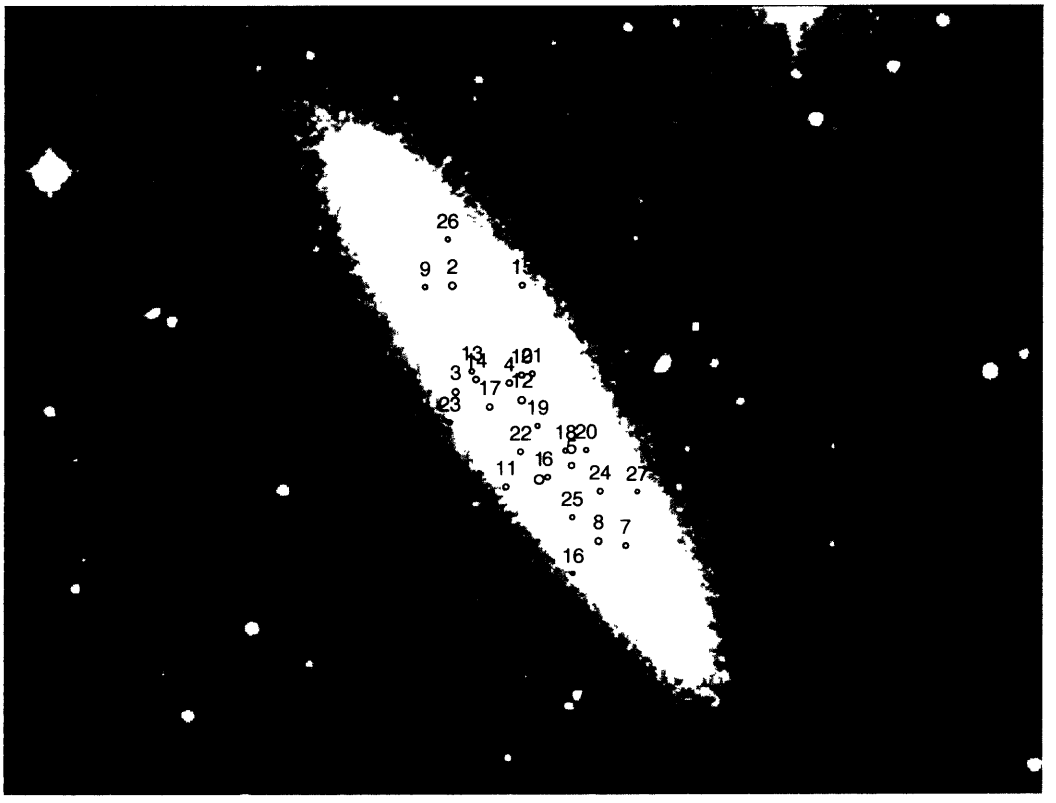

Figure 4-1: The 27 sources we detected within NGC 3877 are shown on an optical image from the *Space Telescope Science Institute Digital Sky Survey.* SN 1998S is src. 1, the relatively large circle next to src. 6. What may appear like 'the number "101" are srcs. 10 and 21. Src. 4 is at the galaxy's center.

away from the aim-point less likely, thus decreasing the value of ρ_{out}. At a separation of $3'$ (the limit to our region of interest), however, this off-axis effect is almost negligible (a factor of ~ 2 reduction in sensitivity[34]).

The second method we employed to estimate the number of background objects used results from a deep (120 ks) field survey[39], which provides an empirical relation between observation flux sensitivity and the density of background sources:

$$N(>S) = 1200 \left[\frac{S}{2 \times 10^{-15}\,\mathrm{erg\,s^{-1}\,cm^{-2}}} \right]^{-1.0\pm0.20} \quad \mathrm{sources\,deg^{-2}}, \tag{4.1}$$

where S is the energy flux.

We used the smallest detected flux, $S = 0.72 \times 10^{-15}\,\mathrm{erg\,s^{-1}\,cm^{-2}}$ (see Sec. ??), in Eq. 4.1. This gave us an estimate of $\lesssim 5$ background objects.

4.3 Counts

We ran *dmextract* to get the background-subtracted photon counts of each source in the soft (0.5-1.2 keV), hard (1.2-8 keV) and broad (0.5-8 keV) energy bands. Table A.2 summarizes the results.

The small number of counts made Poisson statistics untenable. We therefore used approximate error-estimation formulas from a paper by Neil Gehrels[40], aptly titled "Confidence Limits for Small Numbers of Events in Astrophysical Data." All error bars correspond to 1σ.

4.4 Count Rates

Observed counts are not a good way to describe the time evolution of sources because they depend on the amount of exposure the source received. Counts must be divided by exposure to get "count rates."

4.4.1 Auxiliary Response Files

Two factors affect a source's exposure. First is the exposure time of the observation. It is the same for every source within an observation. Second is the combined telescope/filter/detector area described by the source, its effective area. Since effective area is position and energy dependent, it differs for every source.

A source's effective area ($\mathrm{cm^2}$) is stored as a function of energy in its Auxiliary Response File (ARF). The file also contains the quantum efficiency (QE) of the pixel where the source was detected. Quantum efficiency is the fraction of incident photons that a pixel registers and is also energy dependent. It is in units of counts/photon.

The effective area and QE are multiplied together to create the source's ARF, which is a function of energy and in units of cm^2 counts/photon.

We made ARFs for each source using *mkarf*. ARFs were corrected for the degradation of quantum efficiency since launch with *apply_acisabs*.

4.4.2 Effective Count Rates

We calculated effective count rates by dividing the number of detected counts by the exposure time and average ARF:

$$\text{Eff. Count Rate} = \frac{\text{Counts}}{\text{Exposure Time} \times \langle ARF \rangle}. \tag{4.2}$$

Table A.3 summarizes these results.

4.5 Long-Term Variability

To study source evolution we compared their effective count rates in each observation. Each source's effective count rate varied from observation to observation. We characterize this variability by the weighted variance[2], as given in the right-most column of Table A.3. Fig. B-1 shows each source's effective count rates over time.

We find 15 sources (58[3] percent) to be variable. These are sources 5, 8, 9, 10, 12, 14, 16, 17, 19, 20, 21, 22, 24, 26 and 27.

4.6 Source Color

X-ray sources (and most other astrophysical objects) are commonly assigned a "color" that characterizes their emission. Within a given energy range, sources whose emis-

[2]The weighted variance for a sample x is given by $\sqrt{\langle x^2 \rangle - \langle x \rangle^2} / \langle x \rangle$

[3]Excluding the supernova.

sion is dominated by higher/lower energy photons are considered hard/soft. Color quantifies the hardness or softness of the emission.

We employed two methods to determine source colors. First we calculated the hardness ratio of each source. This method used a fixed energy value (1.2 keV) to divide counts into two energy bands (soft and hard). The hardness ratio (ratio of hard-to-total counts) describes the color.

Secondly we employed a new technique called *Quantile Analysis* which has been shown to be superior to hardness ratios when studying low-count sources[41]. Quantile Analysis does not use fixed energy bands. Instead, it uses the energy value that split counts into a predetermined ratio of the total counts. The energy values, or "quantiles," that divide the counts describe emission's color.

4.6.1 Hardness ratios

In deference to low-count statistics, we defined hardness ratios as the ratio of hard (> 1.2 keV) to total counts. This avoided ambiguities incurred with other definitions (e.g. hard/soft) by keeping ratios within a finite and convenient (0 to 1) range. This definition also kept Gehrels errors finite[4].

Table A.4 lists the hardness ratios of each source over the 5 observations.

Fig. B-3 plots hardness ratios against effective count rate. There appears to be no correlation between color and intensity; i.e., brighter sources aren't any harder or softer than faint sources. Furthermore, we see no correlation between hardness ratio and intensity in individual sources. Fig. B-5 plots hardness ratios against effective count rate for each source.

[4]For example, a source with 3 hard and 0 soft counts has a hardness ratio $= 1.0^{+0.00}_{-0.46}$. A hard/soft hardness ratio, on the other hand, would yield a lower limit of 1.18 but an unbounded upper limit, along with the infinite value.

4.6.2 Quantile Analysis

Quantile Analysis[41] involves the energy values E_q that split counts into q and $100-q$ percent of the total counts. For example, E_{25} has 25 percent of counts below it and 75 percent above. We used the median energy, E_{50}. The higher the median value, the harder the source.

Table A.5 lists the median energies of each source over the 5 observations.

Fig. B-4 plots source color against effective count rate. We again see no correlation between color and brightness. Furthermore, we see no correlation between median energy and intensity in individual sources. Fig. B-7 plots median energy against effective count rate for each source.

4.7 Power

We detect sources because they emit energy (photons). The rate at which they emit energy (power) tells us about their inner working, much of which we don't understand.

We infer a source's power output (luminosity) from the power registered on a detector (flux).

4.7.1 Flux

Fluxes (ergs s^{-1} cm^{-2}) of low-count sources are usually determined by a simple scaling of count rates. Such a scaling, however, is problematic because it does not account for spectral color. For example, a hard source has a higher flux than a soft source with the same count rate because its photons are more energetic.

We determined fluxes with a slightly more sophisticated method that incorporates source color. We assumed an absorbed power-law spectrum for each source and modeled them as such in the spectral fitting package *XSPEC*[42]. We ran the *fakeit* command to simulate long (10^6s) observations, using different power-law indices. We

determined the flux using the power-law index which yielded the observed hardness ratio.

We began by assuming that each source emits as a power-law, and that this radiation undergoes photo-electric absorption as it moves through space:

$$A(E) = e^{-\mathrm{N}_H/\sigma(E)} \times \kappa \left(\frac{E}{1\ \mathrm{keV}}\right)^n \quad \text{photons keV}^{-1}\ \text{cm}^{-2}\ \text{s}^{-1}, \tag{4.3}$$

where E[keV] is photon energy, N_H[atoms/cm^2] is the Hydrogen column density, σ[cm^2] are the *XSPEC*-defined photo-electric cross sections based on Balucinska-Church and McCammon[43], κ[photons/keV/cm^2/s at 1 keV] is a normalization constant, and n is the dimensionless power-law index.

We set $\mathrm{N}_H = 1.36 \times 10^{21}$ cm^{-2}[31], $\kappa = 1$, and varied n from 0 to 2 in increments of 0.1. We set the energy range to 0.5 keV $\leq E \leq$ 8.0 keV.

XSPEC combined the source's ARF(E) and $A(E)$ to yield an energy spectrum, photon count, and flux:

$$\text{Spectrum}(E) = A(E) \times \text{ARF}(E) \times 10^6\,\text{s} \quad \text{counts keV}^{-1}, \tag{4.4}$$

where 10^6 s was the length of the simulation. The spectrum gives the number of counts in a bin of width ΔE at a an energy E. XSPEC uses an energy resolution of $\Delta E = 1$ eV.

The number of counts within a given energy range is the sum of the counts in each bin over that energy range,

$$\text{Counts} = \sum_E \text{Spectrum}(E) \times \Delta E \quad \text{counts}. \tag{4.5}$$

We noted the index whose simulation yielded a ratio of hard (>1.2 keV) to total counts that matched the observed hardness ratio. XSPEC used this index to calculate the simulated flux:

$$\text{Simulated Flux} = \frac{\sum_E \text{Spectrum}(E) \times E \times \Delta E}{10^6\,\text{s} \times \sum_E \text{ARF}(E)} \quad \text{keV cm}^{-2}\,\text{s}^{-1}, \tag{4.6}$$

where the numerator is the total detected energy, the denominator is the total detection area, and 10^6s was the length of the observation.

To translate the simulated flux into an "observed" flux we normalized for observation length. And since Eq. 4.6 is in units of simulated photons we also normalized for observed photon counts:

$$\text{Flux} = \frac{\text{Counts}}{\text{Sim. Counts}} \times \frac{10^6\text{s}}{\text{Exp. time}} \times \text{Sim. Flux} \quad \text{keV cm}^{-2}\,\text{s}^{-1}, \tag{4.7}$$

where exposure time refers to the length of the actual observations.

Table A.6 lists the calculated fluxes of each source. We estimated the errors associated with the resultant flux by comparing it to the fluxes computed using the limiting power-law indices (i.e., 0 and 2). We found a ~20 percent difference, and thus assign an error of 20 percent on each flux.

4.7.2 Luminosity

Luminosity is the total power emitted by the source. If we assume that the emission is isotropic, luminosity is related to the flux by the source-detector distance:

$$\text{Luminosity} = 4\pi d^2 \times \text{Flux}. \tag{4.8}$$

The distance to NGC 3877 has been quoted as 17 Mpc[31], but current estimates of Hubble's constant now imply a distance of $d = 12.62 \pm 0.22\,\text{Mpc}$, where we used $H_0 = 71\,\text{km}\,\text{Mpc}^{-1}\,\text{s}^{-1}$ and NGC 3877's redshift[44] $z = 2.99 \pm 0.01 \times 10^{-3}$.

Table A.7 lists the estimated luminosities of each source. We assign a systematic error of 20 percent on each luminosity.

Table 4.1: Normalization factors used to compare XLFs. Consecutive columns give the galaxy, classification type, distance in units of Mpc, apparent diameter in units of arcmin, diameter in kpc, and relative size to NGC 3877 as given by the square of the ratio of the diameters. We used the relative sizes as the normalization factor.

			Diameter		
Galaxy	Type	Distance	Apparent	Geometric	Size
NGC 3877	Sc	12.6 ± 0.22[44]	5.5	10.1	1
M81	Sb	3.6 ± 0.34[45]	26.9	14.1	0.5 ± 0.10
Milky Way	Sbc	—	—	31 ± 3[46]	0.11 ± 0.03

4.8 X-ray source populations

Log(N)-Log(S) curves and X-ray luminosity functions (XLFs) describe the X-ray source population of galaxies. They relate the number of sources exceeding a given flux (luminosity).

We constructed XLFs for each observation. Fig. B-9 shows the XLFs. The sixth plot compares our 5 XLFs to best-fit, normalized XLFs from the Milky Way[1] and M81[2]. We only compare the XLFs of 3877 to two other galaxies because of a lack of time to do a more complete job. We normalized XLFs according to their galaxy's relative size to NGC 3877 in order to account for our assumption that larger galaxies have more stars. Diameters were taken from the NASA/IPAC Extragalactic Database (NED)[5]. Normalization factors are listed in Table 4.1.

NGC 3877's luminous ($L_X \gtrsim 10^{37}\,\mathrm{erg\,s^{-1}}$) source density is higher than that of the other two galaxies. Errors in the normalization factors are dominated by the uncertainties in distance.

4.9 Source Identification

We can make no firm statements about the nature of the X-ray sources. We believe the galaxy's X-ray population consists of XRBs and supernova remnants[46]. Acting

[5]http://nedwww.ipac.caltech.edu

on that assumption, we tentatively classify sources according to their luminosity, variability and color. We acknowledge $\sim$ 5 sources may be background AGNs. We know for certain that source 1 is SN 1998S.

4.9.1 X-ray Binaries

We identify as XRBs those sources that show some long-term variability. These are black holes (BH) and neutron stars (NS).

NS or BH: sources 2, 3, 5, 6, 7, 8, 9, 10 and 13.

Source 4's coincidence with the galactic center makes it a good candidate of being the central engine. It could, however, also be a confluence of a few unresolved low mass X-ray binaries (LMXBs).

Chapter 5

Discussion

We conclude by describing the significance and limitations of our results.

5.1 Sources

Analysis of five *Chandra* observations of NGC 3877 over a 646-day period yielded 27 X-ray sources, including SN 1998S. The nature of the X-ray sources could not be confidently identified. A crude classification scheme employing luminosity and variability suggests a few X-ray binaries. We further associate src. 4 with the central engine, though we acknowledge the source could instead be a confluence of unresolved X-ray sources, likely low-mass X-ray binaries[46], near the galactic center.

Many sources show interesting properties. Src. 12 has a count rate in the second observation that is more than five times its count rate in other observations. Src. 14 got brighter and brighter over an 18-month period, increasing its count rate by more than a factor of 15 in that time.

5.2 Variability

We consider 15 of the 27 X-ray sources to be variable over the 2-year timescale of the observations. This fraction of variable sources is consistent with findings in other galaxies[47].

5.3 Color-Brightness Relations

We see no correlation between color and intensity, neither in the entire population nor for any individual X-ray source.

We do, however, note a decrease in the scatter of color with increasing brightness. Sources with count rates less than $\sim 2 \times 10^{-6}\,\mathrm{counts\,cm^{-2}\,s^{-1}}$ range from very hard to very soft. Sources with count rates greater $\sim 2 \times 10^{-6}\,\mathrm{counts\,cm^{-2}\,s^{-1}}$ have a more confined (about half) color range.

5.4 Population

We find a higher density of bright sources ($L_x \gtrsim 10^{37}\,\mathrm{erg\,s^{-1}}$) in NGC 3877 than we find in two other galaxies, including the Milky Way, as illustrated by the normalized X-ray luminosity functions in Fig. B-9.

NGC 3877's XLFs intersect, suggesting they have different slopes. If so, this complicates the practice of classifying and characterizing galaxies on the basis of their XLFs. A more conclusive characterization of our XLFs requires a Kolmogorov-Smirnov (KS) test.

Appendix A

Tables

Table A.1: The 27 X-ray sources. Consecutive columns give the X-ray source, its right ascension (RA) in units of hours, minutes and seconds; its declination (DEC) in units of degrees, minutes and seconds; and whether or not it was detected in Obs. 1-5 and a merged image. Detections are indicated by "x" and non-detections are indicated by "o".

Src	RA	DEC	Obs 1	Obs 2	Obs 3	Obs 4	Obs 5	Merged
1	11:46:06.1	47:28:55.5	x	x	x	x	x	x
2	11:46:10.5	47:30:23.9	x	x	x	x	x	x
3	11:46:10.1	47:29:34.6	x	x	x	x	x	x
4	11:46:07.6	47:29:39.8	x	x	x	x	x	x
5	11:46:04.6	47:29:02.7	x	x	x	x	x	x
6	11:46:05.7	47:28:56.8	x	x	x	x	x	x
7	11:46:02.0	47:28:26.5	x	x	x	x	x	x
8	11:46:03.2	47:28:28.0	x	x	x	x	x	x
9	11:46:11.7	47:30:22.7	x	x	x	x	x	x
10	11:46:07.1	47:29:43.8	o	o	x	x	x	x
11	11:46:07.6	47:28:51.4	x	x	x	x	x	x
12	11:46:07.0	47:29:32.1	o	x	o	x	o	x
13	11:46:09.4	47:29:44.5	x	x	x	x	x	x
14	11:46:09.2	47:29:40.8	o	o	o	x	x	x
15	11:46:07.2	47:30:25.5	o	x	x	x	o	x
16	11:46:04.3	47:28:12.4	o	x	x	x	x	x
17	11:46:08.5	47:29:28.3	o	o	x	x	o	x
18	11:46:04.9	47:29:09.5	o	x	x	x	o	x
19	11:46:06.3	47:29:20.5	o	o	o	x	o	x
20	11:46:04.0	47:29:10.2	x	o	o	x	x	x
21	11:46:06.6	47:29:44.5	o	x	x	o	o	x
22	11:46:07.0	47:29:08.1	o	o	x	o	x	x
23	11:46:10.3	47:29:20.4	o	o	o	o	o	x
24	11:46:03.3	47:28:51.2	o	x	o	o	o	x
25	11:46:04.5	47:28:38.5	o	o	o	o	o	x
26	11:46:10.8	47:30:45.4	o	x	o	o	o	o
27	11:46:01.6	47:28:51.8	o	o	x	o	o	o

Table A.2: Source counts. Consecutive columns give the X-ray source and the number of counts detected during Obs. 1–5.

Src	Obs 1	Obs 2	Obs 3	Obs 4	Obs 5
1	607	689	487	565	315
2	25	26	29	32	31
3	13	25	22	30	28
4	19	23	15	28	26
5	17	10	16	20	23
6	15	21	16	20	13
7	13	14	9	18	17
8	11	8	12	9	21
9	9	16	8	8	9
10	3	8	11	12	11
11	9	9	7	11	7
12	0	31	2	6	4
13	7	5	7	10	11
14	0	3	1	14	21
15	4	5	7	6	6
16	1	8	4	6	8
17	0	3	20	1	3
18	4	5	6	6	4
19	3	4	5	10	3
20	5	2	5	8	1
21	0	17	2	0	0
22	0	1	7	5	4
23	2	3	1	1	1
24	0	7	0	0	0
25	0	2	2	2	1
26	0	5	0	0	1
27	0	0	3	0	0

Table A.3: Effective count rates. Consecutive columns give the X-ray source, its effective count rates in Obs. 1–5, and the weighted variance of its count rate sample. Effective count rates are in units of 10^{-7} counts cm^{-2} s^{-1}.

Src	Obs 1	Obs 2	Obs 3	Obs 4	Obs 5	Variance
1	1070	950	800	635	390	9.20
2	44	36	48	36	38	0.07
3	22	35	36	34	35	0.10
4	33	32	25	31	32	0.03
5	30	14	26	24	29	0.16
6	26	28	26	22	16	0.10
7	23	19	15	21	21	0.04
8	20	11	20	10	27	0.27
9	16	22	13	9	11	0.19
10	5	11	18	13	14	0.19
11	16	13	12	12	9	0.05
12	0	43	3	7	4	2.71
13	12	7	12	11	14	0.05
14	0	4	2	16	26	1.28
15	7	7	12	7	7	0.05
16	2	11	7	7	10	0.19
17	0	4	33	1	4	2.33
18	7	7	10	7	5	0.04
19	6	6	8	11	4	0.11
20	9	3	8	9	1	0.24
21	0	24	3	0	0	1.95
22	0	1	11	6	5	0.43
23	4	4	2	1	1	0.09
24	0	9	0	0	0	0.95
25	0	3	3	2	1	0.09
26	0	7	0	0	1	0.57
27	0	0	5	0	0	0.50

Table A.4: Hardness ratios. Consecutive columns give the X-ray source, its hardness ratios in Obs. 1–5, and the variance of its hardness ratio sample. Hardness ratios are defined as the ratio of hard-to-total counts. Ratios for sources with 0 counts are ill-defined and indicated by "—".

Src	Obs 1	Obs 2	Obs 3	Obs 4	Obs 5	Var
1	0.6	0.6	0.7	0.6	0.6	0.06
2	0.6	0.8	0.7	0.7	0.7	0.06
3	0.7	0.5	0.7	0.7	0.7	0.13
4	0.4	0.3	0.4	0.5	0.4	0.21
5	0.7	0.9	0.8	0.6	0.7	0.15
6	0.5	0.5	0.7	0.7	0.7	0.12
7	0.9	0.8	1.0	0.8	0.8	0.10
8	0.8	0.6	0.9	0.7	0.8	0.14
9	0.7	0.6	1.0	1.0	1.0	0.20
10	0.7	0.6	0.9	0.8	0.6	0.15
11	0.6	1.0	0.4	0.7	0.7	0.28
12	—	0.6	0.5	0.2	1.0	0.53
13	1.0	1.0	1.0	1.0	1.0	0.00
14	—	0.7	0.0	1.0	0.9	0.61
15	0.5	0.4	0.7	0.7	0.7	0.20
16	0.0	0.4	0.3	0.5	0.6	0.61
17	—	0.0	0.2	0.0	0.3	1.06
18	0.8	1.0	0.8	0.8	0.8	0.11
19	0.7	1.0	0.6	0.8	1.0	0.20
20	0.6	0.5	0.2	0.5	1.0	0.46
21	—	0.6	0.5	—	—	0.08
22	—	1.0	0.0	0.2	0.3	1.05
23	1.0	1.0	1.0	1.0	1.0	—
24	—	0.1	—	—	—	—
25	—	0.0	0.5	0.0	0.0	1.73
26	—	0.2	—	—	1.0	0.67
27	—	—	1.0	—	—	—

Table A.5: Median X-ray energies. Consecutive columns give the X-ray source and the median energy of its registered X-ray counts in Obs. 1–5. Energies are in units of keV. Sources with no counts are indicated by "—".

Src	Obs 1	Obs 2	Obs 3	Obs 4	Obs 5
1	1.5	1.4	1.6	1.4	1.3
2	1.5	1.7	1.8	1.8	1.6
3	1.4	1.2	1.4	1.4	1.8
4	1.0	1.0	1.0	1.2	0.9
5	1.3	2.0	1.5	1.3	2.1
6	1.5	1.2	1.4	1.5	1.7
7	2.5	1.6	1.9	1.7	1.5
8	1.5	1.9	2.0	2.7	1.9
9	1.5	1.5	2.5	2.4	1.7
10	1.7	1.5	1.7	1.5	2.1
11	1.2	1.6	0.9	1.6	1.9
12	—	1.5	1.3	1.0	3.4
13	3.0	2.1	3.4	3.0	3.6
14	—	3.7	0.7	2.7	2.8
15	1.9	0.6	2.1	1.3	1.3
16	0.7	1.1	1.0	1.1	1.5
17	—	0.9	0.8	0.7	0.8
18	2.3	2.6	1.6	1.9	3.4
19	1.9	1.7	1.4	1.6	3.4
20	1.5	2.1	0.9	1.2	3.2
21	—	1.5	1.4	—	—
22	—	1.3	0.8	0.8	0.9
23	2.6	3.1	2.8	5.7	4.9
24	—	0.7	—	—	—
25	—	1.0	1.0	0.8	0.5
26	—	0.9	—	—	2.0
27	—	—	2.7	—	—

Table A.6: Flux estimates. Consecutive columns give the X-ray source and its estimated fluxes in Obs. 1–5. Fluxes are in units of 10^{-15} erg cm^{-2} s^{-1}. We assign a systematic error of 20 percent on each flux.

Src	Obs 1	Obs 2	Obs 3	Obs 4	Obs 5
1	308.4	248.0	240.8	155.7	81.4
2	11.7	12.2	19.1	14.0	12.1
3	5.5	6.2	8.7	8.1	12.4
4	3.5	3.4	3.3	5.2	3.9
5	6.7	6.5	7.7	4.9	13.2
6	7.8	5.5	6.5	6.2	5.5
7	12.8	5.8	6.4	7.2	5.8
8	5.6	4.8	9.5	5.8	10.5
9	4.7	6.7	7.2	4.7	3.9
10	1.8	3.2	6.3	3.6	6.2
11	2.8	4.1	1.3	4.0	3.6
12	0.0	11.5	0.7	0.8	3.5
13	8.2	3.4	8.7	7.0	10.4
14	0.0	3.6	0.1	8.9	14.7
15	2.9	2.7	5.4	1.5	1.6
16	0.1	1.8	0.8	1.1	2.7
17	0.0	0.4	2.9	0.4	0.4
18	3.7	4.1	3.1	2.9	3.5
19	2.6	2.0	2.1	3.3	2.8
20	2.5	1.4	0.9	1.8	0.8
21	0.0	6.9	0.9	0.0	0.0
22	0.0	0.3	0.9	0.6	0.6
23	2.1	2.8	1.0	2.0	1.6
24	0.0	0.2	0.0	0.0	0.0
25	0.0	0.4	0.4	0.2	0.5
26	0.0	0.7	0.0	0.0	0.5
27	0.0	0.0	2.8	0.0	0.0

Table A.7: Luminosity estimates. Consecutive columns give the X-ray source and its luminosities in Obs. 1–5. Luminosities are in units of $10^{38}\,\mathrm{erg\,s^{-1}}$. We assign a systematic error of 20 percent on each luminosity.

Src	Obs 1	Obs 2	Obs 3	Obs 4	Obs 5
1	58.6	47.1	45.7	29.6	15.5
2	2.2	2.3	3.6	2.7	2.3
3	1.0	1.2	1.7	1.5	2.4
4	0.7	0.7	0.6	1.0	0.7
5	1.3	1.2	1.5	0.9	2.5
6	1.5	1.0	1.2	1.2	1.0
7	2.4	1.1	1.2	1.4	1.1
8	1.1	0.9	1.8	1.1	2.0
9	0.9	1.3	1.4	0.9	0.7
10	0.3	0.6	1.2	0.7	1.2
11	0.5	0.8	0.3	0.8	0.7
12	0.0	2.2	0.1	0.2	0.7
13	1.6	0.6	1.7	1.3	2.0
14	0.0	0.7	0.0	1.7	2.8
15	0.6	0.5	1.0	0.3	0.3
16	0.0	0.3	0.1	0.2	0.5
17	0.0	0.1	0.6	0.1	0.1
18	0.7	0.8	0.6	0.5	0.7
19	0.5	0.4	0.4	0.6	0.5
20	0.5	0.3	0.2	0.3	0.2
21	0.0	1.3	0.2	0.0	0.0
22	0.0	0.1	0.2	0.1	0.1
23	0.4	0.5	0.2	0.4	0.3
24	0.0	0.0	0.0	0.0	0.0
25	0.0	0.1	0.1	0.0	0.1
26	0.0	0.1	0.0	0.0	0.1
27	0.0	0.0	0.5	0.0	0.0

Appendix B

Figures

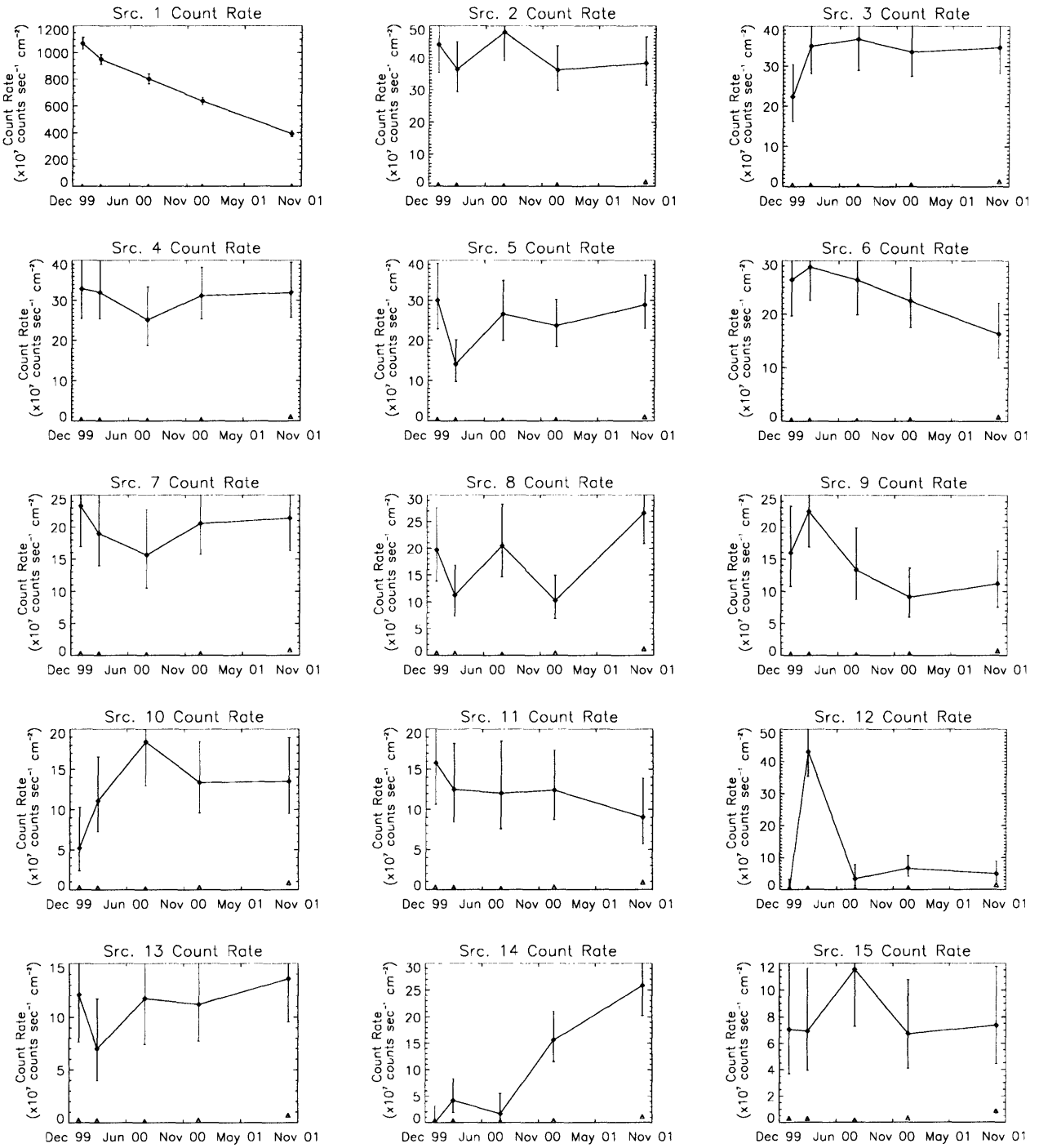

Figure B-1: Count rates over time, or variability, of sources 1-15.

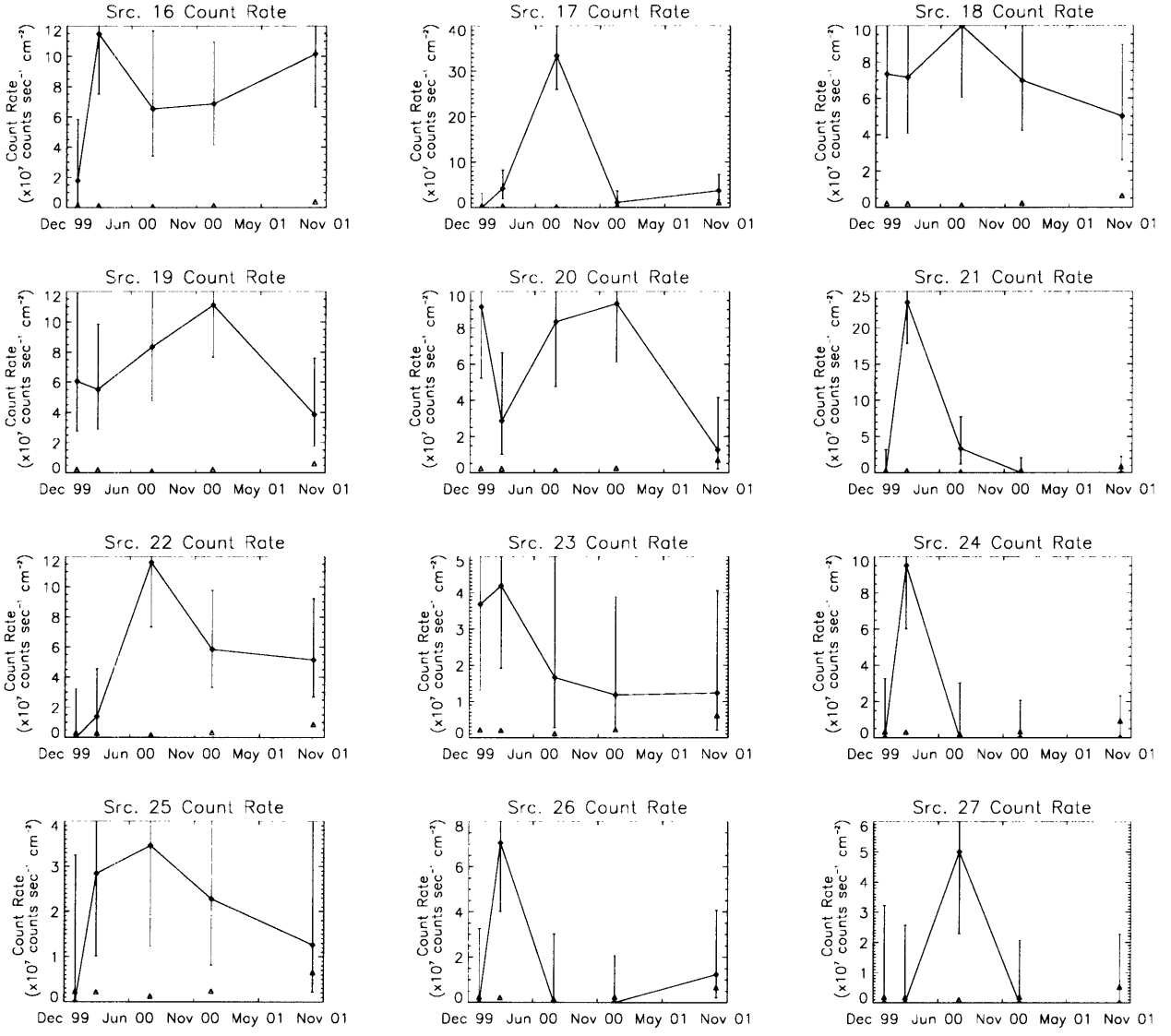

Figure B-2: Variability of sources 16-27.

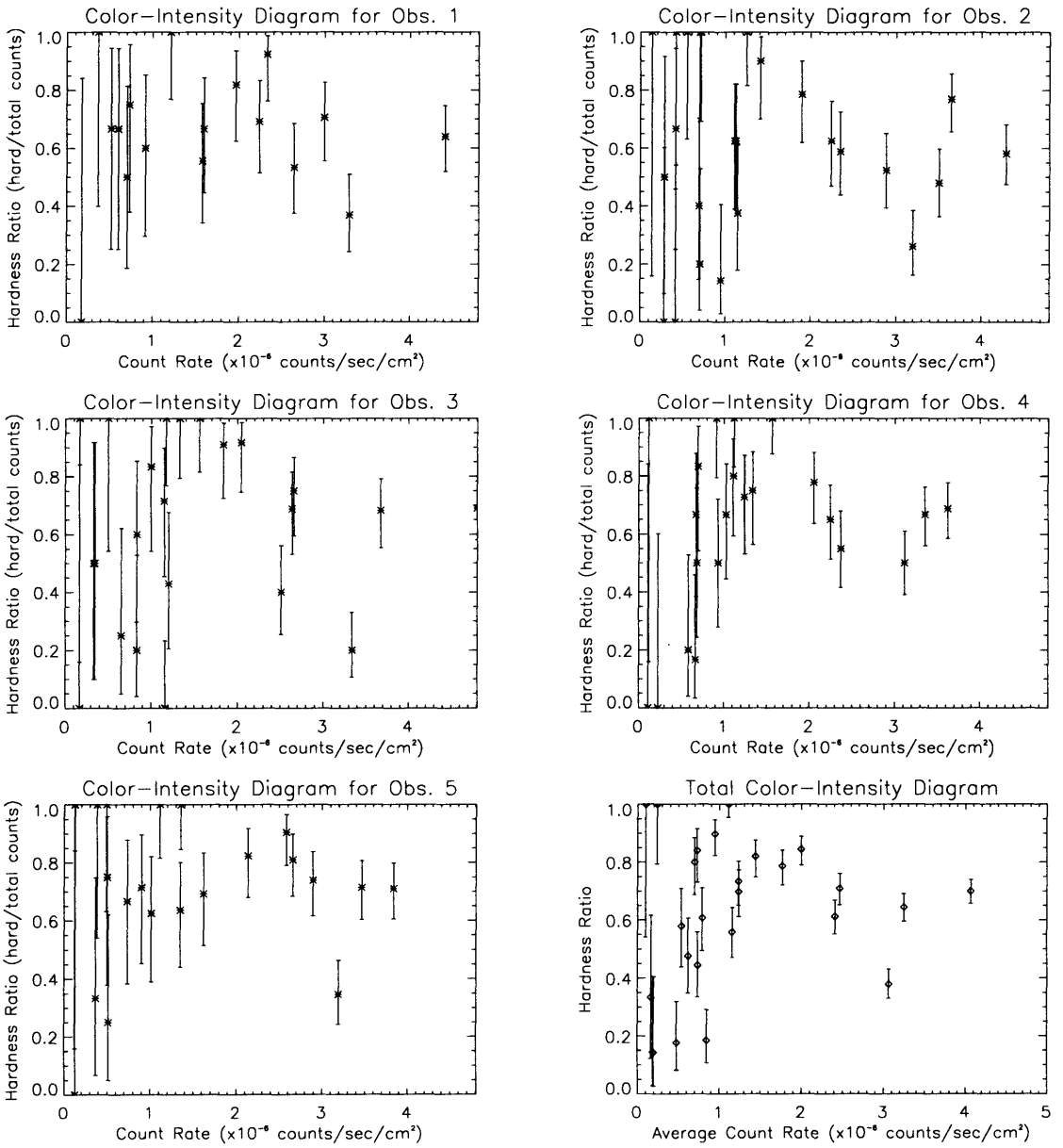

Figure B-3: Color-intensity diagrams of each observation. There appears to be no relation between intensity and hardness ratio.

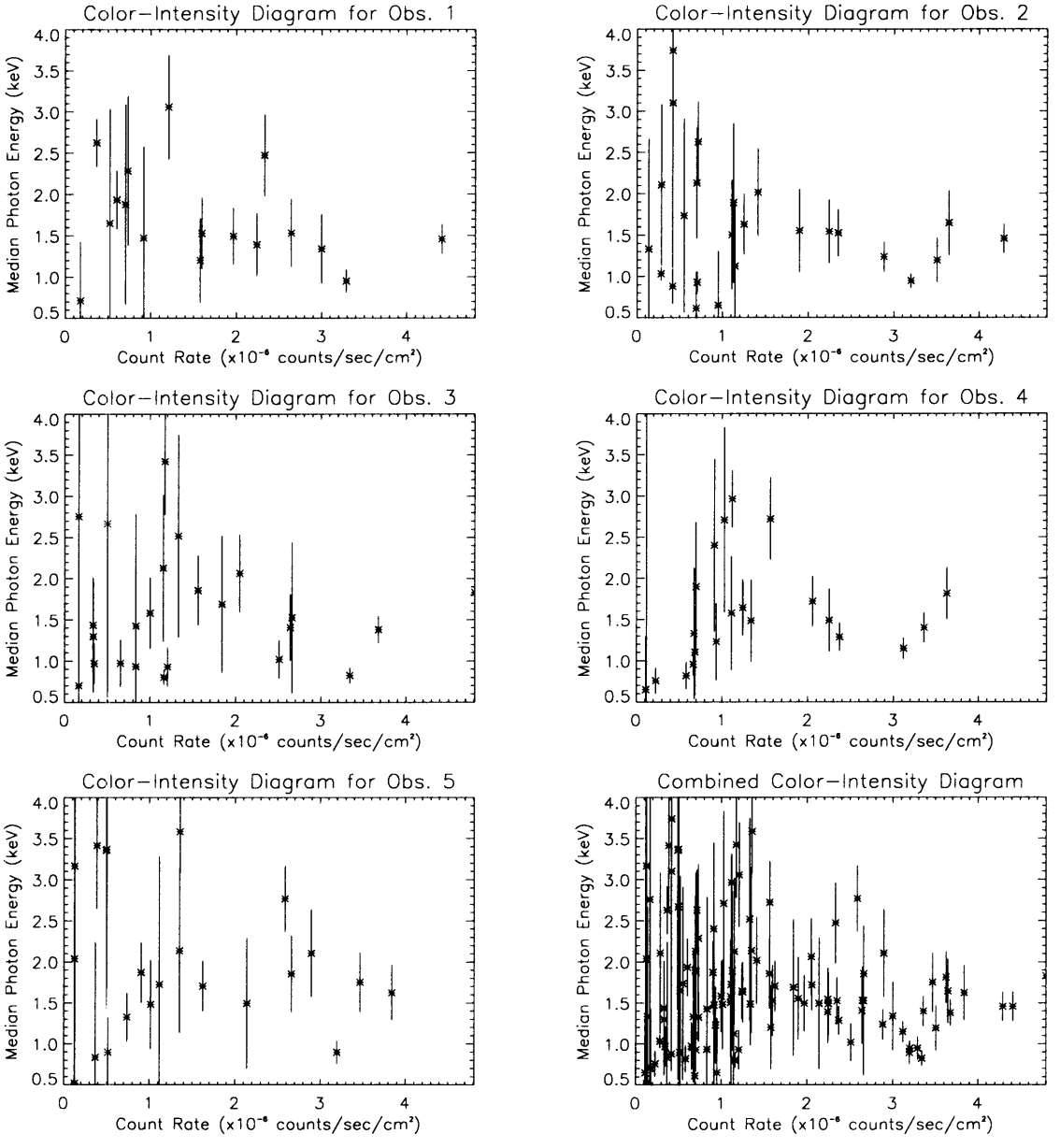

Figure B-4: Color-intensity diagrams of each observation. There appears to be no relation between intensity and median energy.

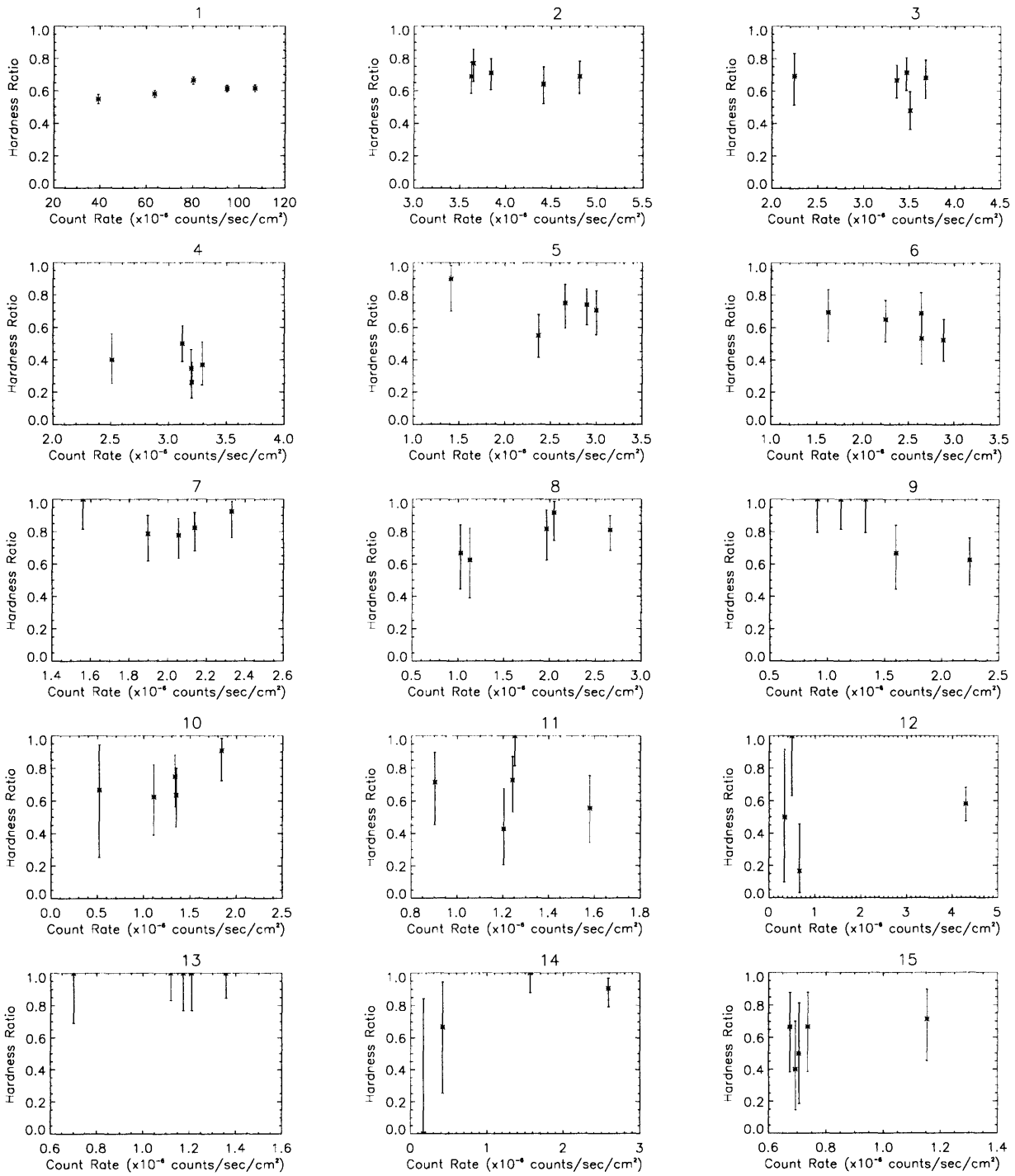

Figure B-5: Hardness ratio-intensity diagrams for sources 1-15.

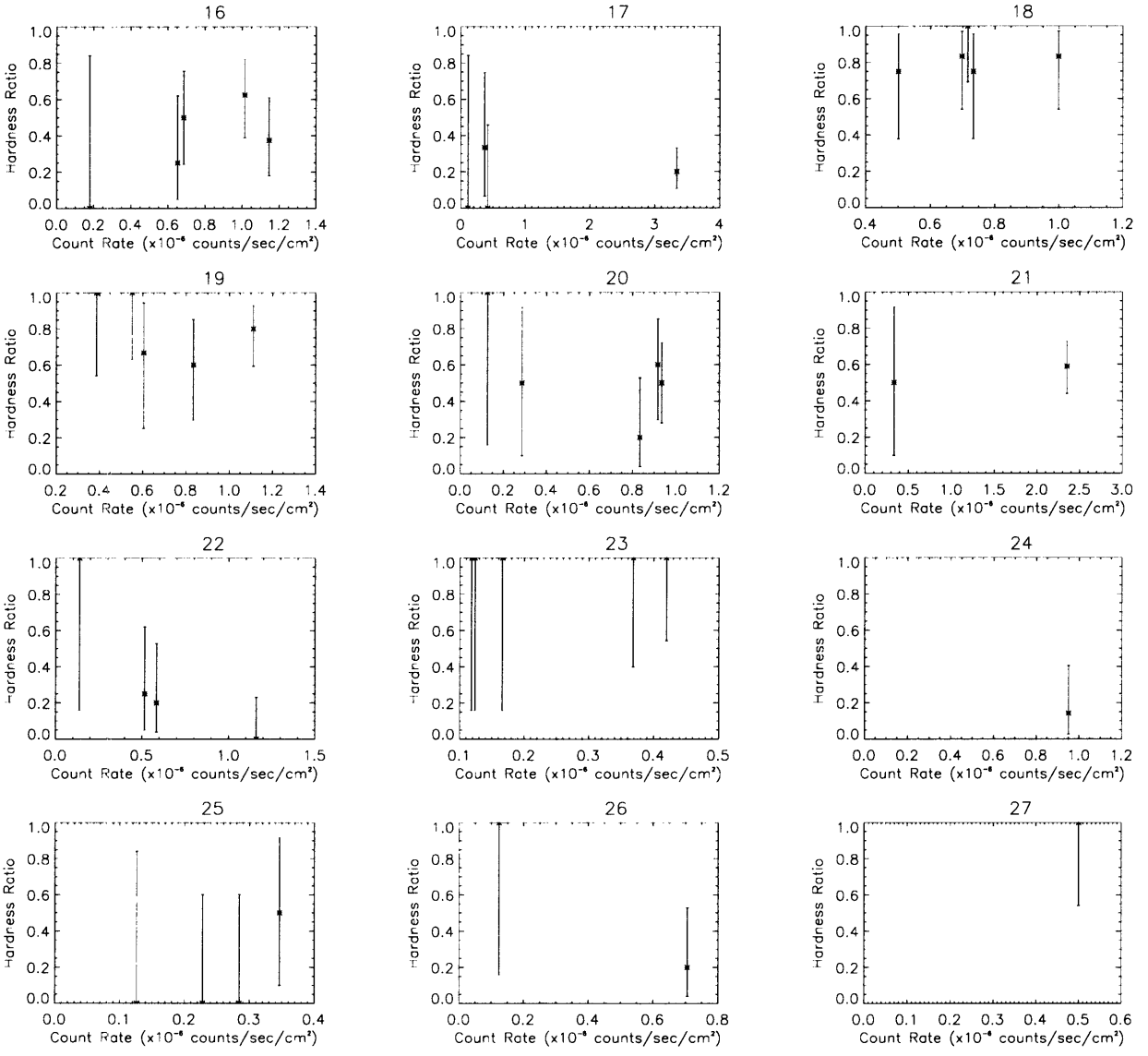

Figure B-6: Hardness ratio-intensity diagrams for sources 16-27.

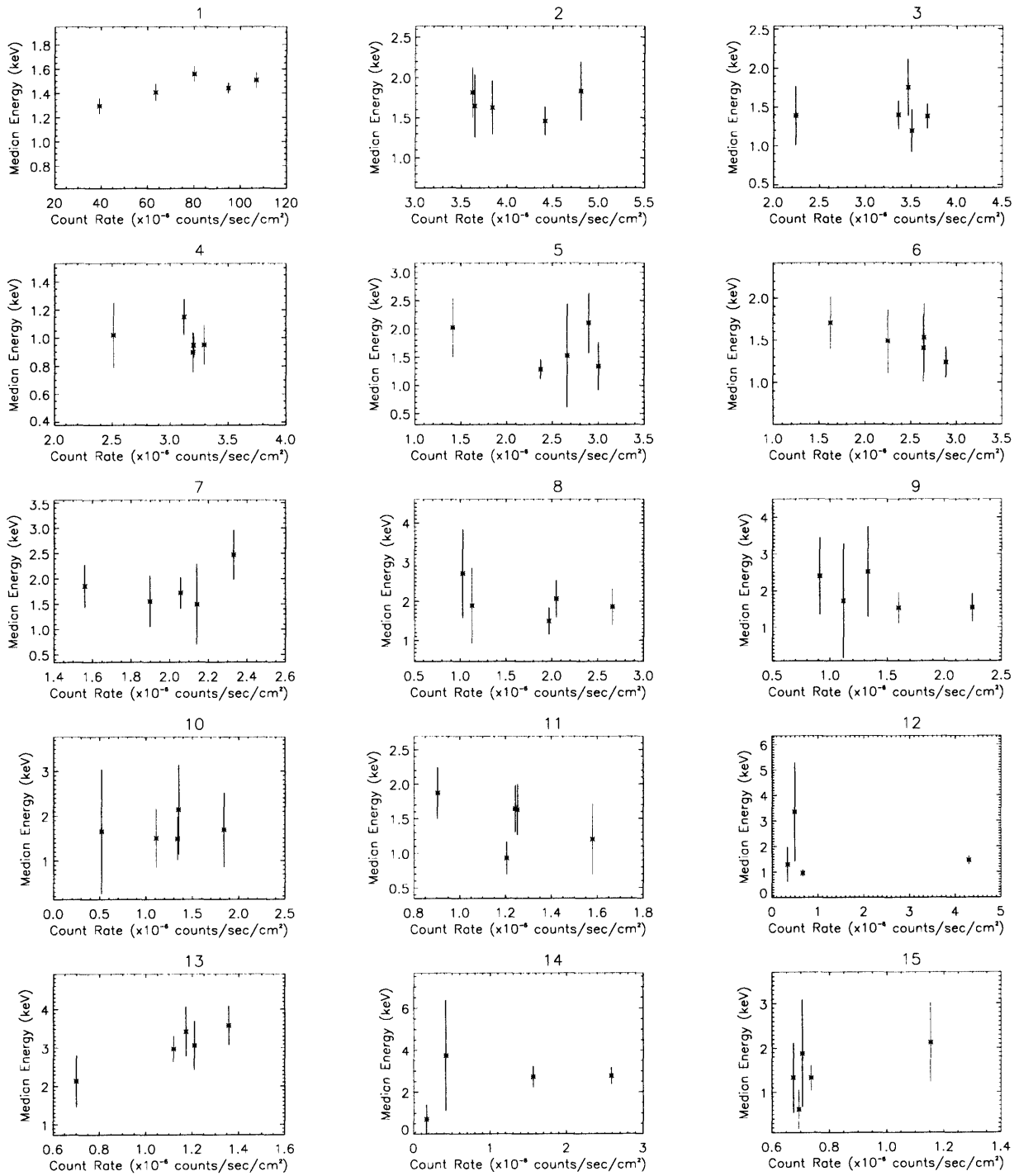

Figure B-7: Median energy-intensity diagrams for sources 1-15.

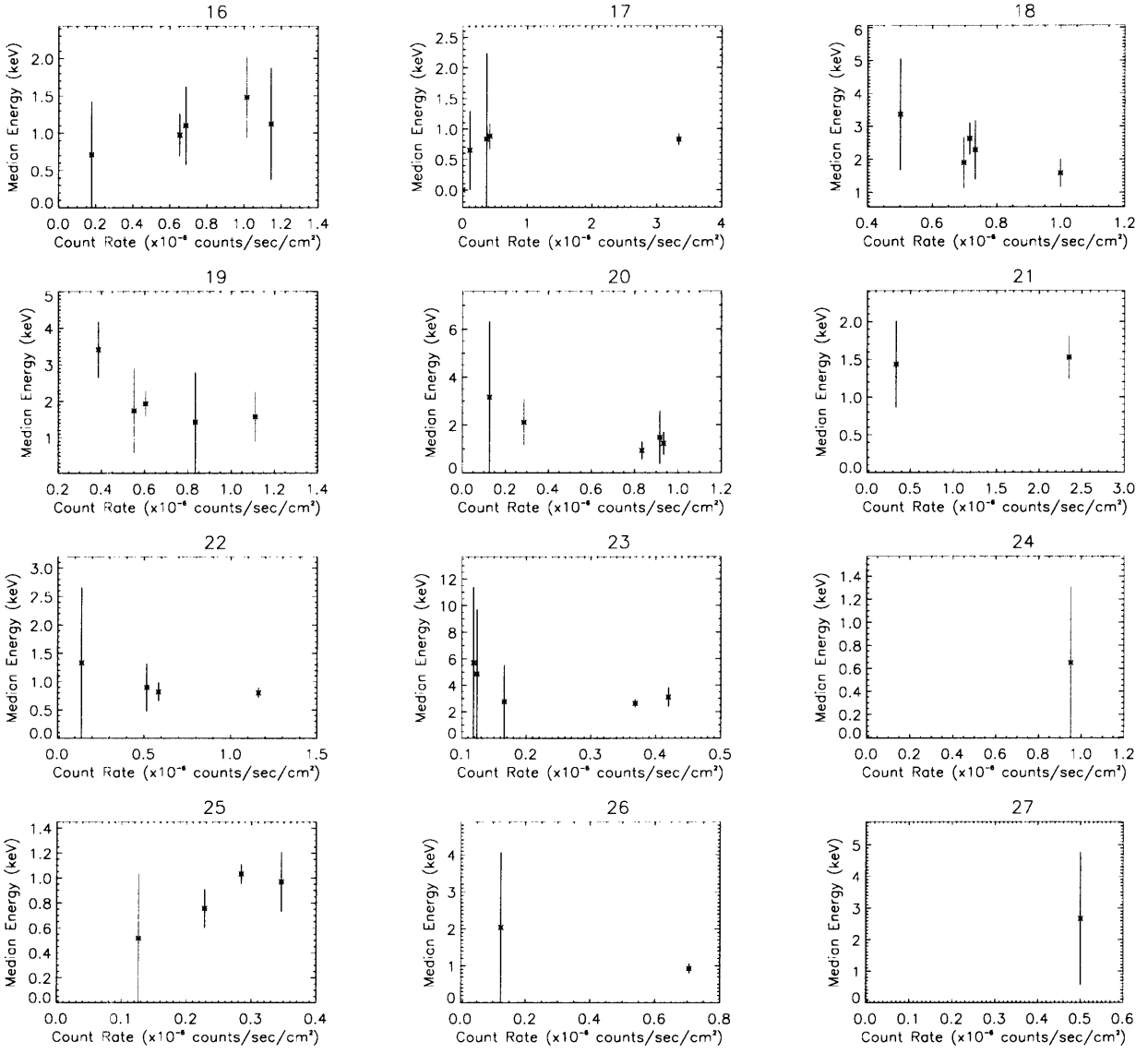

Figure B-8: Median energy-intensity diagrams for sources 16-27.

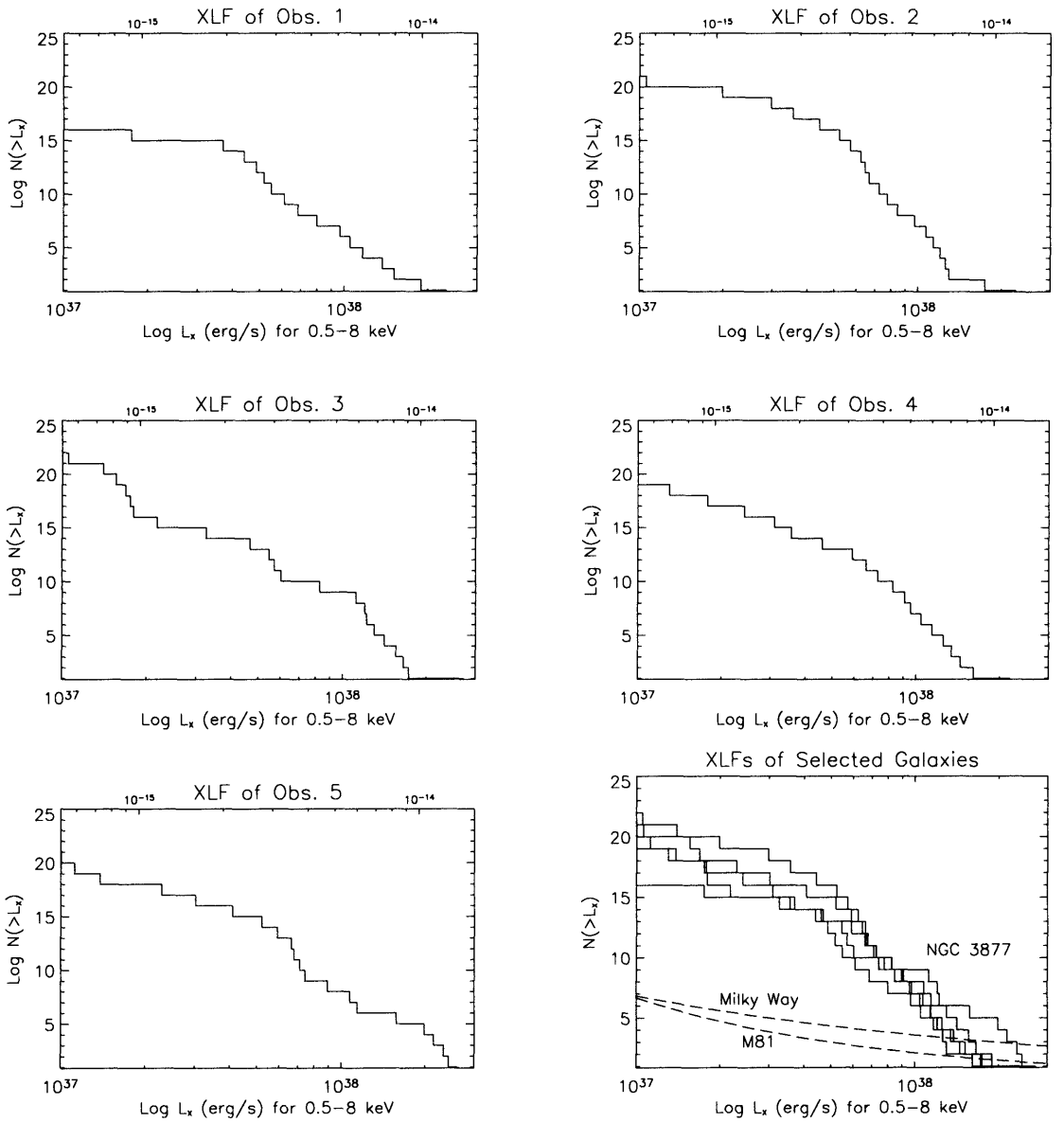

Figure B-9: X-ray luminosity functions. The bottom axis gives luminosity in units of $\mathrm{erg\,s^{-1}}$and the top axis gives flux in units of $\mathrm{erg\,cm^{-2}\,s^{-1}}$. We show XLFs from the five observations. We also compare them to best-fit, normalized XLFs from the Milky Way[1] and M81[2]. The normalization procedure is described in the text.

Bibliography

[1] H.-J. Grimm, M. Gilfanov, and R. Sunyaev. The Milky Way in X-rays for an outside observer. Log(N)-Log(S) and luminosity function of X-ray binaries from RXTE/ASM data. *Astronomy and Astrophysics*, 391:923–944, September 2002.

[2] A. F. Tennant, K. Wu, K. K. Ghosh, J. J. Kolodziejczak, and D. A. Swartz. Properties of the Chandra Sources in M81. *The Astrophysical Journal*, 549:L43–L46, March 2001.

[3] Scott Sewell. *X-ray Physics.* M.I.T. Department of Physics, Cambridge, MA 02139, version 1.26 edition, January 2003.

[4] Philip A. Charles and Frederick D. Seward. *Exploring the X-ray Universe*, chapter 3, pages 65–68. Cambridge University Press, New York, 1st edition, 1995.

[5] Wallace Tucker and Karen Tucker. *Revealing the Universe. The Making of the Chandra X-ray Observatory.* Harvard University Press, Cambridge, Ma., 1st edition, 2001.

[6] Philip G. Judge, Stanley C. Solomon, and Thomas R. Ayres. An Estimate of the Sun's ROSAT-PSPC X-ray Luminosities Using SNOE-SXP Measurements.

[7] H. Friedman, S. W. Lichtman, and E. T. Byram. Photon Counter Measurements of Solar X-rays and Extreme Ultraviolet Light. *The Physical Review*, 83:1025–1030, May 1951.

[8] Philip A. Charles and Frederick D. Seward. *Exploring the X-ray Universe*, chapter 1, page 2. Cambridge University Press, New York, 1st edition, 1995.

[9] R. Giacconi, H. Gursky, F.R. Paolini, and B. Rossi. Evidence for x Rays From Sources Outside the Solar System. *Physical Review Letters*, 9:439–443, December 1962.

[10] S. Bowyer, E. T. Byram, T. A. Chubb, and H. Friedman. X-Ray Emission from the Direction of Scorpius. *Astronomical Journal*, 69:135–+, 1964.

[11] Philip A. Charles and Frederick D. Seward. *Exploring the X-ray Universe*, chapter 1, page 5. Cambridge University Press, New York, 1st edition, 1995.

[12] H. Gursky, R. Giacconi, P. Gorenstein, J. R. Waters, M. Oda, H. Bradt, G. Garmire, and B. V. Sreekantan. A Measurement of the Location of the X-Ray Source SCO X-1. *The Astrophysical Journal*, 146:310–316, October 1966.

[13] S. Bowyer, E. T. Byram, T. A. Chubb, and H. Friedman. Cosmic X-ray Sources. *Science*, 147:394–398, 1965.

[14] A. Sandage, P. Osmer, R. Giacconi, P. Gorenstein, H. Gursky, J. Waters, H. Bradt, G. Garmire, B. V. Sreekantan, M. Oda, K. Osawa, and J. Jugaku. On the optical identification of SCO X-1. *The Astrophysical Journal*, 146:316–+, October 1966.

[15] S. Bowyer, E. T. Byram, T. A. Chubb, and H. Friedman. Lunar Occulation of X-ray Emission from the Crab Nebula. *Science*, 146:912–917, November 1964.

[16] H. Friedman, E. T. Byram, and T. A. Chubb. Distribution and Variability of Cosmic X-Ray Sources. *Science*, 156:374–378, April 1967.

[17] H. Mark, R. Price, R. Rodrigues, F. D. Seward, and C. D. Swift. Detection of X-Rays from the Large Magellanic Cloud. *The Astrophysical Journal*, 155:L143+, March 1969.

[18] C. S. Bowyer, M. Lampton, J. Mack, and F. de Mendonca. Detection of X-Ray Emission from 3c 273 and NGC 5128. *The Astrophysical Journal*, 161:L1+, July 1970.

[19] M. Lampton, B. Margon, S. Bowyer, W. Mahoney, and K. Anderson. The X-Ray Spectrum of NGC 5128. *The Astrophysical Journal*, 171:L45+, January 1972.

[20] J. E. Felten, R. J. Gould, W. A. Stein, and N. J. Woolf. X-Rays from the Coma Cluster of Galaxies. *The Astrophysical Journal*, 146:955–958, December 1966.

[21] Philip A. Charles and Frederick D. Seward. *Exploring the X-ray Universe*, chapter 2, page 35. Cambridge University Press, New York, 1st edition, 1995.

[22] B. Ashenbach, H.-M. Hahn, and J. Trumper. *The Invisible Sky. ROSAT and the Age of X-ray Astronomy.* Copernicus, New York, 2nd edition, 1998.

[23] Classifying X-ray Sources in External Galaxies from X-ray Colors. *The Astrophysical Journal*, 595:719–726, October 2003.

[24] S. Immler, Q. Daniel Wang, Douglas C. Leonard, and Eric M. Schlegel. A Deep *Chandra* X-ray Observation of NGC 1637. *The Astrophysical Journal*, 595:727–742, October 2003.

[25] P. Kaaret. A Chandra High Resolution Camera Observation of X-Ray Point Sources in M31. *The Astrophysical Journal*, 578:114–125, October 2002.

[26] A. K. H. Kong, M. R. Garcia, F. A. Primini, S. S. Murray, R. Di Stefano, and J. E. McClintock. X-Ray Point Sources in the Central Region of M31 as Seen by Chandra. *The Astrophysical Journal.*

[27] A. Zezas and G. Fabbiano. *Chandra* Observations of The Antennae Galaxies (NGC 4038/4039). IV. The X-ray Source Luminosity Function and the Nature of Ultraluminous X-ray Sources. *The Astrophysical Journal*, 577:726–737, October 2002.

[28] K. Belczynski, V. Kalogera, A. Zezas, and G. Fabbiano. X-ray Binary Populations: The Luminosity Function of NGC 1569. *The Astrophysical Journal*, 601:L147–L150, February 2004.

[29] Craig L. Sarazin, Jimmy A. Irwin, and Joel N. Bregman. *Chandra* X-ray Observations of the X-ray Faint Elliptical Galaxy NGC 4697. *The Astrophysical Journal*, 556:533–555, October 2001.

[30] M. Gilfanov, H.-J. Grimm, and R. Sunyaev. L_x-SFR Relation in Star-Forming Galaxies. *Monthly Notices of the Royal Astronomical Society*, 347:L57–L60, January 2004.

[31] David Pooley, Walter H. G. Lewin, Derek W. Fox, Jon M. Miller, Christina K. Lacey, Schuyler D. Van Dyk, Kurt W. Weiler, Richard A. Sramek, Alexei V. Filippenko, Douglas C. Leonard, Stefan Immler, Roger A. Chevalier, Andrew C. Fabian, Claes Fransson, and Ken'ichi Nomoto. X-ray, Optical and Radio Observations of the Type II Supernovae 1998em and 1998S. *The Astrophysical Journal*, 572:932–943, June 2002.

[32] W.-D. Li, C. Li, A. V. Filippenko, and E. C. Moran. Supernova 1998S in NGC 3877. *IAU Circ.*, 6829, March 1998.

[33] J. E. Davis. Event Pileup in Charge-Coupled Devices. *The Astrophysical Journal*, 562:575–582, November 2001.

[34] Chandra X-ray Center. *The Chandra Proposers' Observatory Guide*, December 2003.

[35] Science Threads for CIAO 3.0. Technical report, The *Chandra* X-ray Center, April 2004. http://cxc.harvard.edu/ciao/threads; accessed May 1, 2004.

[36] M. Markevitch, M. W. Bautz, B. Biller, Y. Butt, R. Edgar, T. Gaetz, G. Garmire, C. E. Grant, P. Green, M. Juda, P. P. Plucinsky, D. Schwartz, R. Smith,

A. Vikhlinin, S. Virani, B. J. Wargelin, and S. Wolk. *Chandra* Spectra of the Soft X-ray Diffuse Background. *The Astrophysical Journal*, 583:70–84, December 2003.

[37] Maxim Markevitch. ACIS Background. Technical report, The *Chandra* X-ray Center, September 2001. http://cxc.harvard.edu/contrib/maxim/bg; accessed Apr 20, 2004.

[38] P. E. Freeman, V. Kashyap, R. Rosner, and D. Q. Lamb. A Wavelet-Based Algorithm for the Spatial Analysis of Poisson Data. *The Astrophysical Journal Supplement Series*, 138:185–218, January 2002.

[39] R. Giacconi, P. Rosati, P. Tozzi, M. Nonino, G. Hasinger, C. Norman, J. Bergeron, S. Borgani, R. Gilli, R. Gilmozzi, and W. Zheng. First Results from the X-ray and Optical Survey of the *Chandra* Deep Field South. *The Astrophysical Journal*, 551:624–634, April 2001.

[40] Neil Gehrels. Confidence Limits for Small Numbers of Events in Astrophysical Data. *The Astrophysical Journal*, 303:336–346, April 1986.

[41] J. Hong, E. M. Schlegel, and J. E. Grindlay. New Spectral Classification Technique for X-ray Sources: Quantile Analysis.

[42] Keith Arnaud and Ben Dorman. *XSPEC: An X-ray Spectral Fitting Package.* HEASARC, Greenbelt, MD 20771, version 11.3.x edition, October 2003.

[43] M. Balucinska-Church and D. McCammon. Photoelectric absorption cross sections with variable abundances. *The Astrophysical Journal*, 400:699–+, December 1992.

[44] M. A. W. Verheijen and R. Sancisi. The Ursa Major cluster of galaxies. IV. HI synthesis observations.

[45] W. L. Freedman, S. M. Hughes, B. F. Madore, J. R. Mould, M. G. Lee, P. Stetson, R. C. Kennicutt, A. Turner, L. Ferrarese, H. Ford, J. A. Graham, R. Hill, J. G. Hoessel, J. Huchra, and G. D. Illingworth. The Hubble Space Telescope Extragalactic Distance Scale Key Project. 1: The discovery of Cepheids and a new distance to M81. *The Astrophysical Journal*, 427:628–655, June 1994.

[46] Philip A. Charles and Frederick D. Seward. *Exploring the X-ray Universe.* Cambridge University Press, New York, 1st edition, 1995.

[47] Albert K. H. Kong, Rosanne DiStefano, Michael R. Garcia, and Jochen Greiner. *Chandra* Studies of the X-ray Point Source Luminosity Functions of M31. *The Astrophysical Journal*, 585:298–304, March 2003.